Summer 8-2020

Additive manufacturing of binary alloy A phase field approach

Manoj Ghosh

ADDITIVE MANUFACTURING OF BINARY ALLOY

A PHASE FIELD APPROACH

by

Manoj Ghosh, B.Sc.

A Thesis Presented in Partial Fulfillment
of the Requirements of the Degree
Master of Science

COLLEGE OF ENGINEERING AND SCIENCE
LOUISIANA TECH UNIVERSITY

August 2020

LOUISIANA TECH UNIVERSITY

THE GRADUATE SCHOOL

JUNE 10, 2020
Date

We hereby recommend that the thesis prepared under our supervision by **Manoj Ghosh,** B.Sc.

entitled **Additive manufacturing of binary alloy A phase field approach**

be accepted in partial fulfillment of the requirements for the Degree of

Master of Science in Mechanical Engineering

Dr. Kasra Momeni
Supervisor of Thesis Research

Dr. Prahu Arumugam
Head ofMechanical Engineering

Thesis Committee Members:
Dr.Pedro Derosa

Dr. Henry Cardenas

Dr. Hamzeh Bardaweel

Approved:

Hisham Hegab
Director of Engineering & Science

Approved:

Ramu Ramachandran
Dean of the Graduate School

ABSTRACT

A phase-field approach is pursued to study the solidification of binary alloys, and equations governing the kinetics of the phase transformation are derived. The Ginzburg Landau equation and Cahn Hilliard equation were developed for the binary alloy phase-field model, considering both free energy minimization and conservation of mass. The analytical solutions for a dilute solution alloy are derived. For the thin interface limit, the correlation between the phase-field mobility and kinetic interface coefficient is developed, neglecting the diffusivity at the solid side. For a one-dimensional steady-state condition, along with the diffuse interface, the concentration profile is established as a function of interface velocity. The variation of the partition coefficient as a function of interface velocity is shown. Numerical simulations for the diluted solution are used to study the interface velocity is observed as a function of undercooling for the classic sharp interface model, partitionless solidification, thin interface, and sharp interface model.

APPROVAL FOR SCHOLARLY DISSEMINATION

The author grants to the Prescott Memorial Library of Louisiana Tech University the right to reproduce, by appropriate methods, upon request, any or all portions of this Thesis. It is understood that "proper request" consists of the agreement, on the part of the requesting party, that said reproduction is for his personal use and that subsequent reproduction will not occur without the written approval of the author of this Thesis. Further, any portions of the Thesis used in books, papers, and other works must be appropriately referenced to this Thesis.

Finally, the author of this Thesis reserves the right to publish freely, in the literature, at any time, any or all portions of this Thesis.

Author _____

Date _____

DEDICATION

This thesis is dedicated to my parents, who have been my inspiration throughout my whole journey.

TABLE OF CONTENTS

ABSTRACT iii

APPROVAL FOR SCHOLARLY DISSEMINATION iv

DEDICATION v

LIST OF FIGURES viii

LIST OF TABLES x

ACKNOWLEDGMENTS xi

CHAPTER 1 INTRODUCTION 1

1.1 Phase-field approach for microstructure evolution insight 3

CHAPTER 2 BACKGROUND 6

2.1 An overview of the AM process 6

2.2 Microstructure 7

2.2.1 Material and microstructure discontinuities 7

2.2.2 Residual stress 10

2.2.3 Texture 12

2.2.4 Grain structure and morphology 16

2.2.5 Phases 20

2.3 Computational approach 26

CHAPTER 3 ALLOY PHASE FIELD MODEL 28

CHAPTER 4 DILUTE SOLUTION APPROXIMATION 35

CHAPTER 5 ANALYTICAL SOLUTION OF GINZBURG-LANDAU EQUATION 40

CHAPTER 6 THIN INTERFACE LIMIT 45

CHAPTER 7 SOLUTE TRAPPING 50

CHAPTER 8 THERMODYNAMIC EQUILIBRIUM AND STABILITY CONDITION FOR HOMOGENOUS STATE 57

CHAPTER 9 NUMERICAL SIMULATION 60

CHAPTER 10 CONCLUSIONS AND FUTURE WORK 67

APPENDIX A MATLAB AND MOOSE CODES 69

A.1 Common Tangent Plot 69

A.2 Moose Code 70

BIBLIOGRAPHY 82

LIST OF FIGURES

Figure 2-1: Different kinds of defects formed by the AM process due to different process parameters. (a) porosity [30] (b) lack of fusion between layers [31] (c) balling [32] (d) hot tears [33] (e) fish scale [34].....8

Figure 2-2: Residual stress formation (a) heating-phase, (b) cooling-phase [43].....11

Figure 2-3: Variation of maximum residual stress vs. temperature gradient [47]. 12

Figure 2-4: Solidification map for Ti-6Al-4V [53].....14

Figure 2-5: High-resolution EBSD (0.4-lm step size) of (a) α-phase and (b) prior β-phase reconstruction [54] (c) Pole figures showing reconstructed β-textures for Ti-6Al-4V [56].....15

Figure 2-6: (a) Texture by unidirectional scanning [57]. (b) texture by bidirectional scanning [57]. (c) temperature gradient during bidirectional scanning [52]. (d) primary dendrite growth patterns of grains with different orientations by bidirectional laser scanning [52].....16

Figure 2-7: Combined effect of thermal gradient and solidification velocity on solidification microstructure [61]–[64].....17

Figure 2-8: Process map to control (a) solidification microstructure of single bead deposit of Ti64 [53], (b) melt pool dimensions for a single bead deposit of Ti64 [53]. ...18

Figure 2-9: Application of combined cellular automation and finite element modeling simulation tool, predicting microstructural evolution in metals [71]. 20

Figure 2-10: An example of a time-temperature-transformation (TTT) diagram [76]. ...23

Figure 2-11: DSC experiments observations for forward and reverses martensitic phase transformation temperatures from different regions [78]. 25

Figure 2-12: DSC plot for deposited from Ni and Ti powder mixture (1:1.33) after annealing at1050℃ for 10H and aged at (a) 400℃ for 1H and (b) 500℃ for 1H [80]. 26

Figure 5-1: Free energy density curves of solid and liquid against composition.....44

Figure 7-1: Variation of concentration profile for different values of P. 53

Figure 7-2: Variation of partition coefficient as a function of p. 54

Figure 9-1: Variation of interface velocity, calculated at $\xi^* \to \infty$ as a function of TSol-T 62

Figure 9-2: Variation of interface velocity calculated neglecting kinetic effect as a function of ξ^*. 63

Figure 9-3: Variation of solid composition along with the interface. 64

Figure 9-4: Deviation of solid composition along with the interface with dimentionless diffusivity a $D^* = 1$, b $D^* = 2$ c $D^* = 5$ and variation of Υ along with the interface with dimentionless diffusivity a $D^* = 1$, b $D^* = 2$ c $D^* = 5$ 64

Figure 9-5: Deviation of solid composition along the interface with dimentionless diffusivity $D^* = 1$, $D^* = 2$ and $D^* = 5$ for (a) $\beta S0 = 1$ (b) $\beta S0 = 2$. 65

Figure 9-6: Comparison of numerical result with analytical result. 66

LIST OF TABLES

Table 2-1: Mechanical properties for titanium alloy [73].....21

Table 2-2: Summary of solid-phase transformation [75].....22

ACKNOWLEDGMENTS

I would like to express my sincere gratitude and appreciation to my thesis advisor Dr. Kasra Momeni for his continuous guidance, patience, and for all the mentorship provided during the journey. This work would not have been achievable without the financial support from NFS, Louisiana Tech University, and NASA. I would also like to thank people from the MOOSE google group for their suggestions and guidance. I was able to learn and use MOOSE for the project.

Most importantly, I would like to thank family members, including my parents and my sister. Parents are my role model. I would also like to thank my friends and all the Bangladeshi people here in Ruston. Nonetheless, I wish to thank my loving wife, Athai, for her continuous support.

CHAPTER 1

INTRODUCTION

Additive Manufacturing (AM) is one of the efficient production processes that can replenish traditional production technologies. Additive manufacturing is a process of joining materials to make objects from 3D model data, usually layer upon layer [1]. It is generally known as a rapid manufacturing, rapid prototyping, or freedom fabrication method. This process is often indicated as the third industrial revolution. Using the AM process, computer-aided design can be directly transformed into a finished product. Moreover, parts with complex geometries can easily be manufactured by the AM process with almost zero waste. The acceptance of the AM process is confronted by processability and quality issues like flaws caused by distortion, cracks, or permeability. Process parameters can control these issues, where the effect of these process parameters can be investigated through brute force experimentation.

Additive manufacturing processes are classified according to their raw materials: powder-based, liquid-based, and solid-based [2]. One of the most popular AM processes is the laser powder bed fusion, which itself can be classified into selective laser melting (SLM), selective laser sintering (SLS), and electron beam melting (EBM).

The early history of the AM process was started with photo sculpture in the 1860s and topography in the 1890s. These improvements paved the way for the “Photo-glyph

recording" technique, which involves two or three-dimensional records in space [3]. Photo sculpture is highly linked with the additive manufacturing process, and therefore it is highly referenced in AM literature these days. Research efforts in the 1960s and 70s introduce us with the modern AM process photopolymerization in the 1960s, powder fusion in 1972 [4], and sheet lamination in 1979 [5]. The laser beam melting process was introduced in the early 1990s [6]. Due to design flexibility and applicability to a wide variety of materials, interest and investment have increased in AM technologies in recent times. Additive manufacturing of parts commonly requires no finishing processes, which results in nearly zero material loss and therefore reduces the cost of fabrication.

Functionally graded materials (FGM) are inhomogeneous materials where composition and microstructure change gradually, which allows the fabrication of parts with an optimum performance by tailoring material properties as a function of position. Nowadays application of AM process to design and manufacture industrial FGM products is very popular. For discrete material FGM design, to control the gradual change in material properties, each layer is supplied with the desired material composition. On the other hand, for continuous design, constituent material composition is unceasingly controlled [7].

Additive manufacturing processes provide the opportunity to synthesize high-performance materials. Due to post-processing complexities, employing high-performance materials for engineering applications was limited. Postprocessing treatment, like machining, is complicated and costly, and sometimes impossible. The additive manufacturing process requires minimalistic postprocessing, and thus it provides a highly effective fabrication approach for high-performance materials. Using additively manufactured conformal cooled molds made is also cost-effective and time-efficient.

The additive manufacturing process can be further defined as a localized heat source used for melting followed by solidification, which takes place in the presence of inert gas or vacuum atmosphere. Computational modeling, design tools, and process parameters are vital factors for controlling additive manufacturing technologies. These details have a crucial impact on different additive manufacturing technologies. During the AM process, the microstructure is controlled by the heat treatment due to the multiple passes of laser source and other process parameters. There are several ways to model this process and predict the microstructure evolution, which phase field is one of the key methods that is summarized below.

1.1 Phase-field approach for microstructure evolution insight

The microstructure of materials includes grains, where their orientation controls the physical and mechanical properties of materials. Thus, gaining insight into the mechanism of microstructure evolution is essential. The phase-field method is a powerful and versatile tool to simulate microstructure evolution at the mesoscale. The shape and distribution of grains in microstructure are expressed as a function of the phase-field variables. Phase-field variables remain unchanged within the grains—the narrow region, where phase-field variable changes among adjacent grains, is known as interface region. The change in phase-field variables gives the time-dependent evolution of the interface. Reduction in bulk free energy, interfacial energy, and elastic energy are some of the driving forces for microstructure evolution.

In recent years, the phase-field method has become an essential technique to model and study different types of microstructure evolutions. More than a century ago, a liquid-gas model was developed by van der Waals using the interface through which diffusion

takes place [8]. Two continuum equations, popularly known as the Cahn-Hilliard nonlinear diffusion equation [9],[10], and the Allen-Cahn (time-dependent Ginzburg-Landau) equation [11] describe the microstructure evolution. The WBM (Wheeler, Boettinger, and McFadden) phase-field model was later introduced, which deals with isothermal solidification of a binary alloy. In this phase-field model, a free energy surface and field equations were developed for the two types of phase-field variables, i.e., conserved and nonconserved [12]. Later in another study, they considered both local free energy and gradient energy and the impact of solute trapping conditions during rapid solidification [13]. A phase-field model for solutal driven phase transition in the binary alloy was established by Tiaden et al. [14]. A phase-field model for rapid solidification of the binary alloy was presented by Karl Glasner [15] to recover sharp interface laws exhibiting solute trapping by asymptotic analysis.

A general thermodynamically consistent phase-field model for binary alloys was based on entropy function to retain thermodynamic consistency for the non-isothermal system [16]. Non-isothermal dendritic solidification of a binary alloy phase-field model, which includes both temperature and solute redistribution, has been introduced by Loginova et al. [17]. Phase-field simulations for dendrite growth coupled with heat and solute diffusion has been presented for a thin interface [18], [19], where the influence of physical parameters on free dendrite growth was studied. This model is valid for unequal solutal diffusivities in the solid and liquid. The simulated results were compared with a sharp interface analytical solution for a one-dimensional solidification system.

In recent years, a new free energy relation for the phase-field yield crystal model implies that two-point correlations are enough to generate stable cubic lattices [20]. This

model was one of the first approaches that self-consistently model elastic and plastic effects at the atomic scale. Later in another work, a phase-field crystal method for structural transformations in binary alloys was developed [21]. This model also predicted the equilibrium properties of eutectic and peritectic binary alloys in two and three dimensions.

In this study, we lay out a mathematical model of an alloy, and we describe the specific properties and derivations of the phase-field model for pure material that is extended to the binary alloys. Then a dilute solution approximation condition and its analytical solution were derived. The phase-field model for the thin interface limit was remodeled. Then the solute trapping in the phase-field model is observed, and the concentration profile across the interface is plotted as a function of interface velocity. In the final section, numerical simulation for a diluted solution was performed. The effect of diffusivity and coefficient of gradient energy (see Chapter 3) on the equilibrium composition is also studied (see Chapter 9). The interface velocity is also expressed as a function of undercooling.

CHAPTER 2

BACKGROUND

2.1 An overview of the AM process

The additive manufacturing process gives some exceptional features that distinguish it from the conventional manufacturing process. The term “additive manufacturing” was chosen by the American Society for Testing and Materials (ASTM) F42 Committee. Additive manufacturing can be used to manufacture components, heretofore unattainable with traditional manufacturing processes, and to reduce the manufacturing time and cost. The unique features of AM technologies are noted below.

Complex geometric cost: AM technology ensures that the most complex geometries require only minimal postprocessing. Thus, the AM process affords the freedom for the designers to design without the increase in cost.

Accuracy of dimension: Dimensional accuracy is an essential issue for the production process. The additive manufacturing process can be used to manufacture parts that are measured in centimeters and ensure the tolerance capabilities tighter than a few hundredths of a millimeter. The expectation is so high that there is an urgency to establish a new tolerance standard for the AM process, such as the tentative tolerance benchmark [22], proposed by Todd.

Design flexibility: AM process is a layer by layer fabrication approach. So, it gives no restriction for any complex geometry as the AM process does not need any postprocessing to attain a complex geometry. It can distribute material precisely as needed to achieve the design flawlessly. That also makes sure of no material waste or very little waste while fabricating components. Different traditional manufacturing process imposes various constraints in the fabrication process. Whereas additive manufacturing does not have these drawbacks, thus providing the freedom to design any complex shape.

Previously AM processes can be categorized into liquid-based, powder-based, and solid-based [23] processes. ASTM International has classified the AM process into seven major categories: 1. binder jetting; 2. direct energy deposition; 3. material extrusion; 4. material jetting; 5. Powder bed fusion; 6. sheet lamination; and 7. T vat photopolymerization [1].

.

2.2 Microstructure

2.2.1 Material and microstructure discontinuities

Figure 2-1 shows different discontinuities, such as porosity, that occur in the AM process. These defects are due to the chosen process parameters and affect the material properties, e.g., fracture toughness and ductility. Several studies have specified that porosity is typical discontinuity for selective laser melting and electron bed melting fabricated products [24], [25]. The high cooling rate during solidification resulting in trapped gas inside the fabricated part is one of the primary reasons for porosity formation. The excessive input energy results in spherical porosity shown in **Figure 2-1**(a). Different postprocessing steps like stress relief, heat treatment, hot isostatic pressing, and surface

treatment are followed to avoid these discontinuities between layers. In some products like aerospace parts and biomedical structures, a certain level of porosity is desired [26]. For these applications, we need to understand the relation between the process variable and porosity. An ultrasonic sensor for determining the fluctuations in the porosity in metal parts during fabrication on a PBF system was developed [26], [27]. Lack of fusion may occur in the AM process, mainly due to a lack of input energy. If the supplied input energy is not enough, the metal powders are not fully melted; it may result in a lack of fusion. Fusion holes are formed between layers due to low input energy. Lack of fusion is often distributed among the scan track and deposited layers [28], [29].

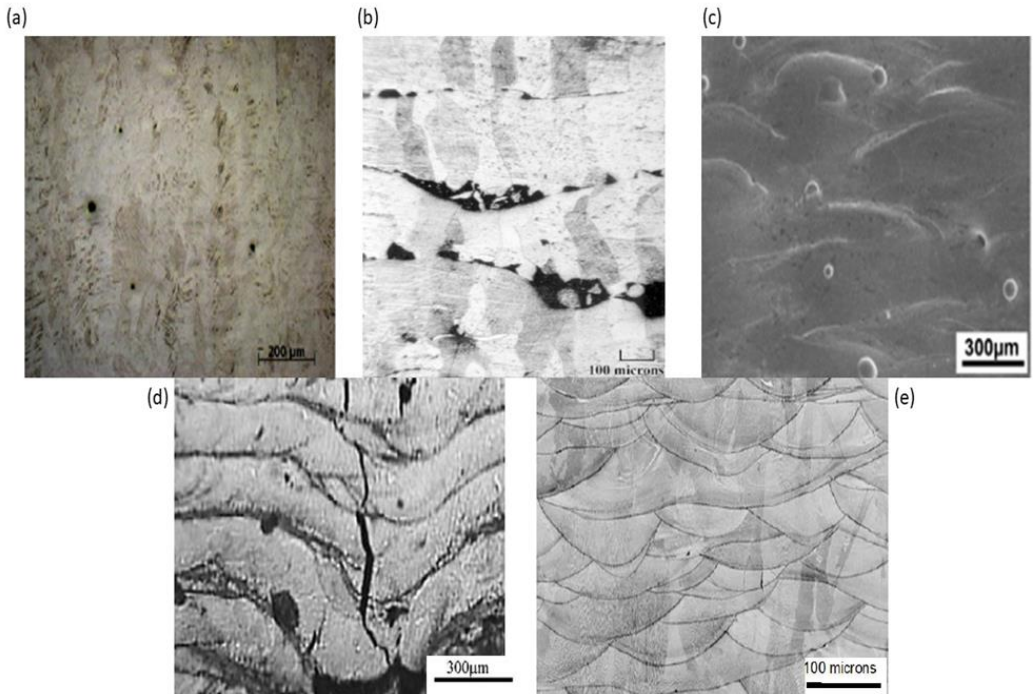

Figure 2-1: Different kinds of defects formed by the AM process due to different process parameters. (a) porosity [30] (b) lack of fusion between layers [31] (c) balling [32] (d) hot tears [33] (e) fish scale [34]

The energy density factor is an important feature in the AM process. The porosity volume fraction can be directly related to the energy density factor. The critical energy

density is dependent on efficiency by which supplied energy is absorbed. The lack of powder particle and low energy density during the AM process may result in porosity [35]. Low energy density causes inhomogeneous mixing and certain types of porosity. On the other hand, high energy densities will result in decreasing surface roughness. Energy density is termed as the average supplied energy per unit volume of deposited material in the AM process. Energy density for SLM process can be expressed as [30],

$$E = \frac{P}{v.h.t} \qquad \textbf{Eq. 2-1}$$

Here P is laser power, v is scanning speed, h is hatch spacing, and t is the layer thickness. A liquid metal will form a spherical shape on a substrate surface, due to surface tension, following the minimum principle of surface energy. This phenomenon is known as a balling effect [36]. Balling results in a rough surface in the solidified layer. Some researchers have shown that the balling effect in the AM process arises with increasing scanning speed due to the significant Marangoni convection [37]. Balling is also caused by high laser energy and may cause deformation in the fabricated part. The laser remelting process can be applied to reduce the balling effect, but that increases the production time [38], [39].

The layer delamination can be caused by thermal effects and sometimes by the oxide formation on the surface. Hot tearing is another source of discontinuities that can be caused by hindered contraction during solidification. Process factors that control these discontinuities can be classified into four major groups: laser related, scan related, powder related, and temperature related. These microstructural discontinuities will severely affect the tensile, fatigue, and other mechanical properties of the fabricated part. Along with

material discontinuities, microstructural discontinuities are also observed due to AM postprocessing.

2.2.2 Residual stress

Residual stress is a stress type that remains in the material. It can be defined as non-uniform plastic deformation in metal from thermal expansion [40] and is considered as a hidden microstructural variable. Residual stress is usually classified according to the scale it occurs. Large residual stress may lead to distortion and unexpected changes in mechanical properties. Atomic dislocation and different coexisting phases in the material may result in residual stress [40]. Residual stress is sometimes desirable, such as a glass plate, as it prevents crack growth in the surface. It can be caused by a temperature gradient mechanism (TGM), which occurs from the thermal gradient around the laser spot. The thermal gradient is introduced due to a localized heat source and slow conduction cooling in AM materials. The microstructure of the material is also controlled by the thermal history of the AM process, and the cool-down phase of the molten top layers, which occurs due to thermal contraction. Underlying material reverses this deformation. It introduces tensile stress at the top layer and compressive stress below.

Many researchers have developed mathematical models to investigate residual stress. Simplified numerical models are used to compare with experimental results [41], where a thinner powder layer thickness was considered in simulations, and the applied energy was adjusted according to the experimental studies. Residual stress in Ti–6Al–4V components has been studied in Ref. [42], using the wire arc AM process. It was revealed that the residual stress is maximum at the wall baseplate transition.

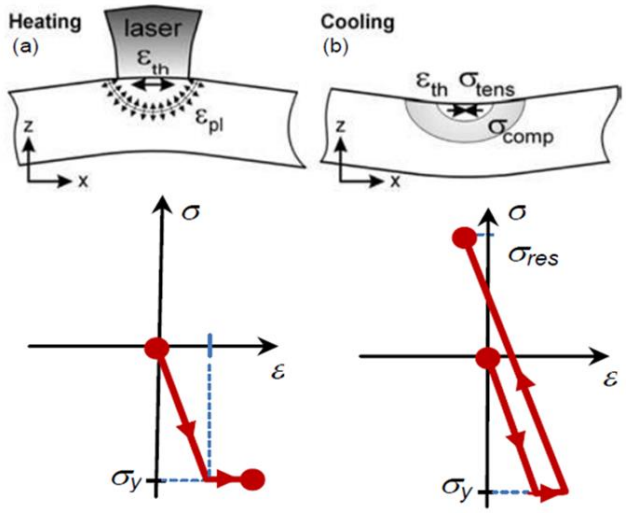

Figure 2-2: Residual stress formation (a) heating-phase, (b) cooling-phase [43].

To control the residual stress, we can modulate the thermal gradient, scanning strategy, and applied loads during the process. IR cameras can be used to monitor the thermal gradient in the PBF process and detect the lack of fusion spot during the process [44], [45]. Two different types of localized preheating approaches were proposed to reduce residual stress [46]. A thermomechanical model was developed to compare these two different approaches. The temperature profile can be a strong parameter to measure residual stress. The models displayed a noticeable decrease in maximum residual stress. **Figure 2-3** shows the relation between a defined temperature gradient and the magnitude of maximum residual stress in a tall wall as the wall cooled down to room temperature [47]. An annealing heat treatment process to eradicate residual stress in additively manufactured Ti-6Al-4V via laser solid forming was presented [48]. During laser solid forming AM process as the deposits were cooled down, the β→α phase transformation took place. An in situ diode annealing in the laser powder bed fusion process to reduce residual stress was developed [49]. A set of laser diodes were used to control the thermal history and thereby reducing

the residual stress. Closed-loop feedback control in PBF is applied to control the thermal gradient that results in residual stress control. In the absence of annealing, residual stress may cause spherical deformation in the powder bed fusion AM process [50]. Different experimental techniques like X-ray diffraction, hole drilling, contour method, and laser line profilometry were proposed to control the effect of various process parameters on residual stress [51]. X-ray diffraction and hole drilling techniques were applied on the surface of the laser powder bed fusion fabricated part. The contour method was applied for residual bulk stress.

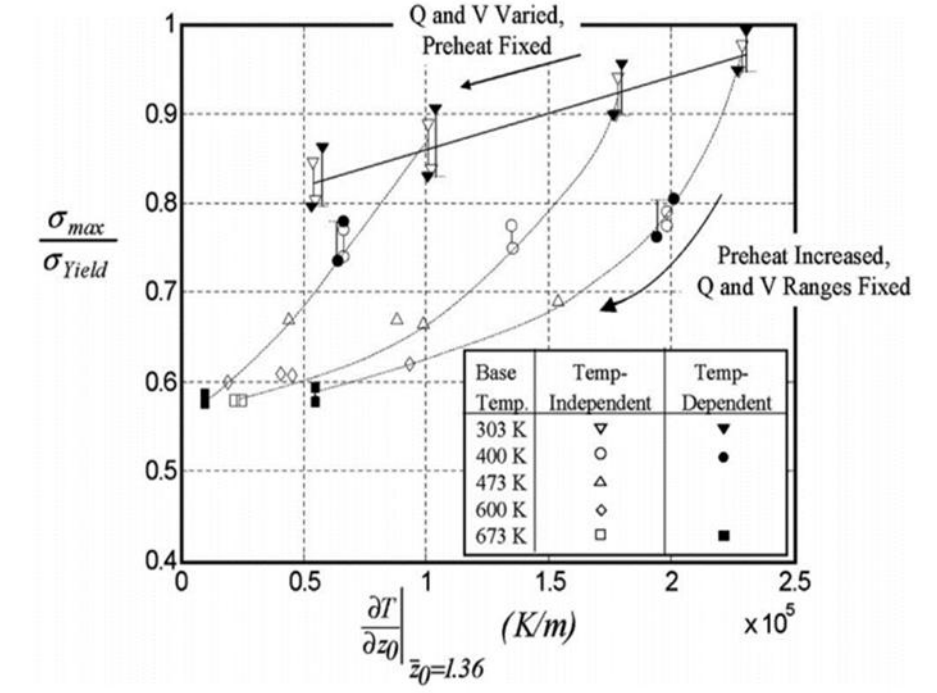

Figure 2-3: Variation of maximum residual stress vs. temperature gradient [52].

2.2.3 Texture

Texture possesses a substantial effect on the mechanical and chemical properties of AM fabricated parts. So, to achieve the desired property in the AM component, texture

control is very important. Researchers have suggested that as the material is deposited, the texture is developed in AM fabricated part. The texture is a macroscale microstructural feature that depends upon the solidification process. The solidification pattern is influenced by the local temperature and grain orientation. The direction of heat flow is normal to the solidification surface and given by, [53]

$$\vec{\nabla}T = \frac{\partial T}{\partial x}\hat{\imath} + \frac{\partial T}{\partial y}\hat{\jmath} + \frac{\partial T}{\partial z}\hat{k} \qquad \textbf{Eq. 2-2}$$

Here, $\hat{\imath}$, $\hat{\jmath}$, and $\hat{k}$ are unit vectors in the scanning (x), width (y), and vertical (z) direction, and T is the temperature. $\vec{\nabla}T$ is the gradient of temperature. G is the magnitude of the gradient [53]. Now,

$$G = ||\nabla T|| = \sqrt{\left(\frac{\partial T}{\partial x}\right)^2 + \left(\frac{\partial T}{\partial y}\right)^2 + \left(\frac{\partial T}{\partial z}\right)^2} \qquad \textbf{Eq. 2-3}$$

At the solid-liquid interface, the solidification rate, R is given by [53],

$$R = U cos\theta \qquad \textbf{Eq. 2-4}$$

The angle, θ, between the direction of heat flow and a horizontal line on the solidification surface (neglecting the Y component) can be calculated from the following relation [53],

$$cos\theta = \frac{\frac{\partial T}{\partial x}}{\sqrt{\left(\frac{\partial T}{\partial x}\right)^2 + \left(\frac{\partial T}{\partial z}\right)^2}} \qquad \textbf{Eq. 2-5}$$

The solidification morphology is calculated from the temperature gradient, G and solidification rate, R. From heat transfer and fluid flow model of AM process, **Eq. 2-2** and **Eq. 2-3** are used to calculate G and R. **Figure 2-4** shows the grain morphology data from G vs. R plot [54].

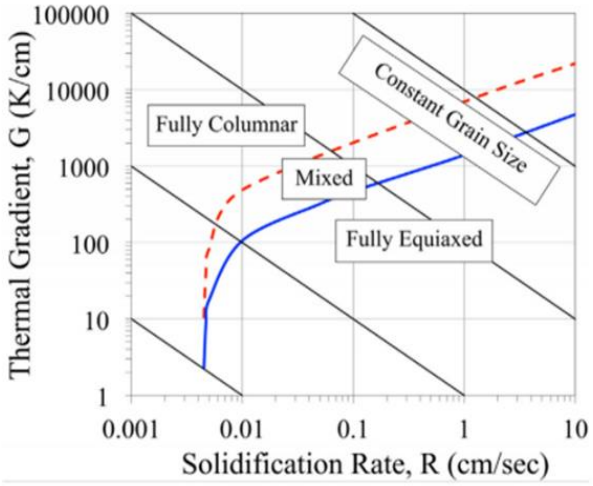

Figure 2-4: Solidification map for Ti-6Al-4V [54]

The effect of low-angle grain boundaries on the predicted grain morphology at the small and large-scale deposition are shown in **Figure 2-5** a and b by the solidification map of Ti-6Al-4V. An experimental approach to study the texture in electron beam melted Ti-6Al-4V has been carried out [55]. Strong texture perpendicular to the build axis revealed as β-phase is reconstructed from α-phase electron backscatter diffraction data. Again the effect of geometry on texture in Ti-6Al-4V alloy has been studied [56]. The reconstruction of the EBSD map indicates the β and α transformation textures that take place due to changes in geometry. **Figure 2-5**c shows the bulk sections grain growth of different layers. It helps to grow coarse grain structure with a texture more optimized with the average growing conditions.

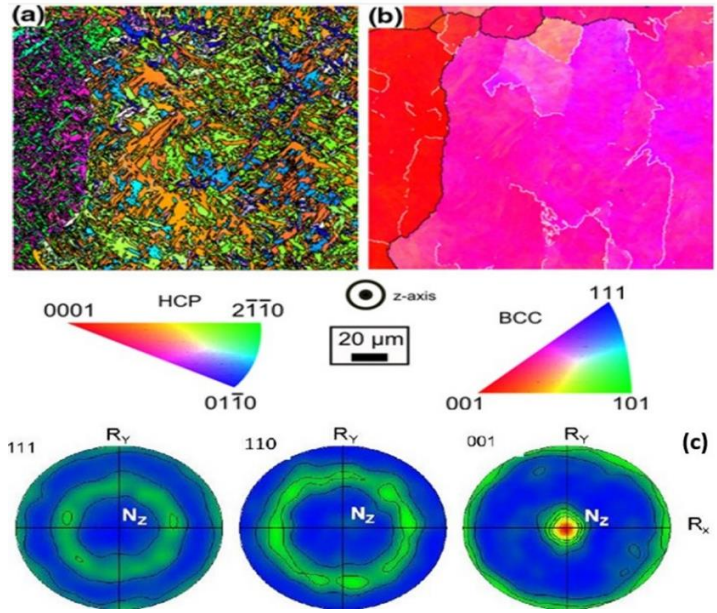

Figure 2-5: High-resolution EBSD (0.4-lm step size) of (a) α-phase and (b) prior β-phase reconstruction [55] (c) Pole figures showing reconstructed β-textures for Ti-6Al-4V [56]

Fiber texture and rotated cube texture is developed by unidirectional and bidirectional laser beam scanning pattern in the AM process. Texture developed by unidirectional and bidirectional scanning direct electron deposition is shown in **Figure 2-6**a and b [57]. At melt pool boundaries, the growth direction of grains and heat flow controls the evolution of texture. When the directions are closely aligned, fiber texture is formed. In the case of misaligned grain growth, cube texture is formed.

Two of the most influential factors for solidification texture are heat flow directions and competitive growth of the grains. Epitaxial growth also plays an important role in the formation of texture. The material tends to grow an epitaxial structure producing columnar grains with <0 0 1> texture along the build direction when solidification occurs. Process parameters like scanning speed and the layer thickness are calibrated to control the texture. The macroscopic scan strategy in the PBF system can also be responsible for the texture.

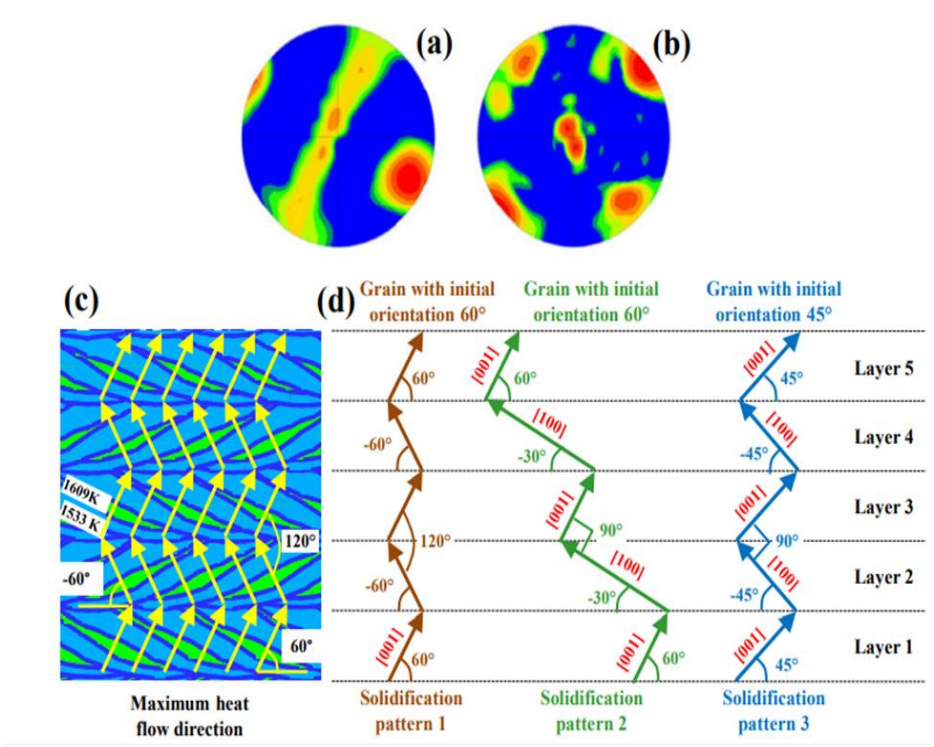

Figure 2-6: (a) Texture by unidirectional scanning [57]. (b) texture by bidirectional scanning [57]. (c) temperature gradient during bidirectional scanning [53]. (d) primary dendrite growth patterns of grains with different orientations by bidirectional laser scanning [53].

2.2.4 Grain structure and morphology

Grain structure plays an important role in solidification cracking and mechanical properties. As the coarsest microstructural features, grains need to be considered. The evolution of microstructure is directly controlled by process parameters [58]. The impact of solidification velocity, temperature gradient, and alloy composition on grain morphology is studied in Ref. [58]. The impact of heat flux on the microstructure of the AM fabricated part was also studied in Ref. [59].

According to the theories of alloy solidification, aside from solidification conditions and material composition, constitutional supercooling defines the solid/liquid interface morphology. Constitutional supercooling occurs with the change of composition

of the solid phase, which causes cooling of liquid below the freezing point at the solidification front. As mentioned in texture, the ratio of thermal gradient G and the kinetics mass transfer R controls the degree of constitutional supercooling. **Figure 2-7** shows the combined effect of G and R on grain morphology. The decrease in G/R ratio results in changing grain morphology in order: planar, cellular, columnar dendritic and equiaxed dendritic. The slope of this plot is defined as [60],

$$Slope = \frac{m_L C_0 (1-k_0)}{k_0 D_L} = \frac{\Delta T}{D_L}, \qquad \textbf{Eq. 2-6}$$

where, m_L = Slope of liquidus curve, k_0 =Equilibrium partition coefficient, ΔT= Equilibrium freezing range, C_0 = Nominal alloy composition, D_L = Solute diffusivity in liquid.

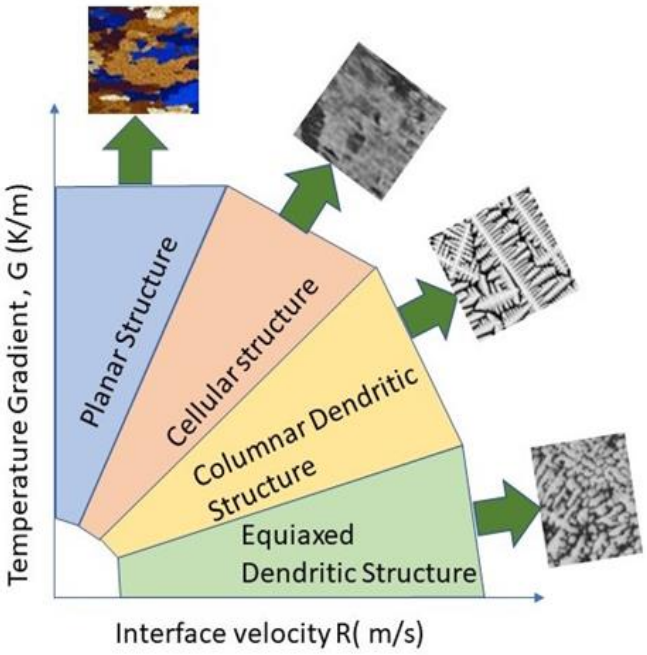

Figure 2-7: Combined effect of thermal gradient and solidification velocity on solidification microstructure [61]–[64].

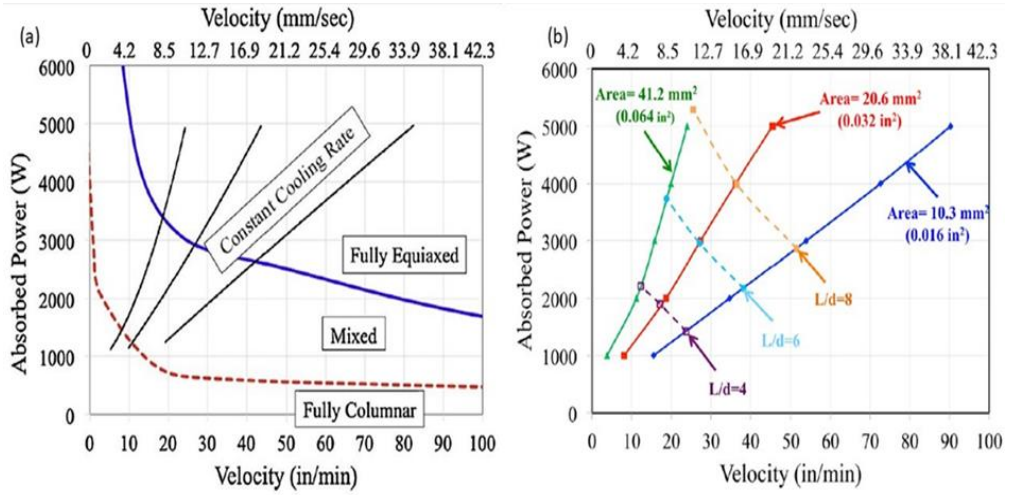

Figure 2-8: Process map to control (a) solidification microstructure of single bead deposit of Ti64 [54], (b) melt pool dimensions for a single bead deposit of Ti64 [54].

In another study, a finite element method was used to develop a solidification process map for single beads deposition of Ti-6Al-4V [54]. By monitoring melt pool dimensions in real-time, in suit microstructure control was possible. For a consistent and predicted net shaped part solidification microstructure and melt pool dimension monitoring, balancing of material feed rate, fine features, and customized smart microstructures are integrated. **Figure 2-8**a shows the process map to control the solidification microstructure in the electron beam process for temperature T= 373K. As the curves of constant cooling rate are almost linear, a constant β grain size can be maintained moving from low powers and low velocities to high power and high velocity. **Figure 2-8**b shows the melt pool dimension control for the electron beam AM process. With the same temperature, this map shows the geometry of a single bead deposited in the middle of a large part.

Different kinds of Ti-alloy plates were fabricated to study the solidification behavior and grain morphology [65]. With the increasing alloying content, volume

fraction, and formation tendency of equiaxed grains in laser additive manufactured Ti-alloy plates increase because of constitutional supercooling and remaining powders in the local melt pool. The presence of columnar grains can affect the mechanical properties and influence the material defect. So, their presence is not desirable in additive manufacturing. Avoiding the presence of columnar grains has been a significant challenge. To favor the formation of equiaxed grains during the wire-based additive manufacturing process of titanium alloys, thermal condition like cooling rate and temperature gradient during solidification were studied [66]. This work demonstrates that potent nuclear particles can facilitate the formation of equiaxed grains.

The consolidation of Ti-6Al-4V powder was also established by combining electron beam additive manufacturing with an isostatic pressing process [67]. Improved mechanical properties are achieved with more equiaxed grains, which have a comparatively smaller grain size than the effective grain size of EBM Ti-6Al-4V. A graded microstructure was manufactured by employing selective melting in some of the internal sections of the sample. For a better understanding of the grain evolution in the metal melting based additive manufacturing process, Cellular Automata-based two-dimensional microstructure model was developed [68]. The relationship between scan pattern and orientation of grain evolution was established. Various cooling rate and thermal gradient show a direct impact on grain size and orientation evolution during the processing of metallic materials.

Figure 2-9 shows a two-dimensional modeling approach combined with a cellular automaton technique to predict the microstructural evolution of grains [69]. Solidification of Fe-C alloy in the molten pool of the LENS laser deposition process was simulated and

observed for dendritic structure. Process conditions like layer thickness, laser speed, and substrate size are shown to have an influential impact on the solidification microstructure. Microstructure modeling of laser deposition using concentrated heat was analyzed [70]. The thermal model was developed to predict realistic deposition geometry. The middle height of the microstructure was pointed as the minimum spacing value by both simulation and experimental studies. The counterbalancing effect of temperature gradient and solidification velocity gives better understanding of the phenomena.

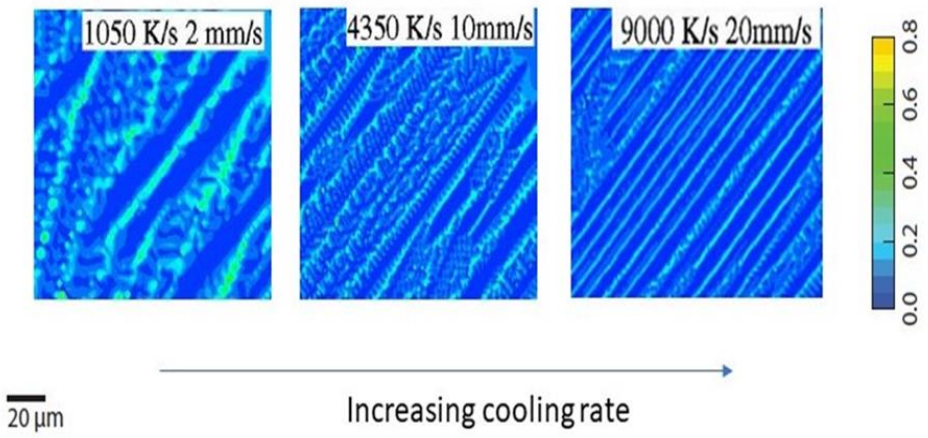

Figure 2-9: Application of combined cellular automation and finite element modeling simulation tool, predicting microstructural evolution in metals [69].

2.2.5 Phases

Multiphase materials are very important for their impact on industrial applications. The additional phase usually makes the multiphase material stronger than single-phase material. The temperature gradient in the additive manufacturing process may result in distortion in the equilibrium structure. In AM products, the large undercooling affects the phases, distribution, and chemical compositions. Both liquid-solid (L→S) and solid-solid (S→S′) transformations have significance in multiphase material. The L→S transformation

determines the distribution of elements within the grains, the S→S′ transformation determines the volume fraction, size, and distribution of second phases present in the microstructure. Due to the localized thermal cycle during additive manufacturing fabrication, AM provides the opportunity to control the liquid-solid phase transformation.

Table 2-1: Mechanical properties for titanium alloy [71].

Alloy	Microstructure	E(GPa)	YS(MPa)	UTS(MPa)
CP-Ti	α	105	692	785
Ti-6Al-4V	α+β	110	850-900	960-970
Ti-6Al-7Nb	α+β	105	921	1024
Ti-5Al-2.5Fe	Metastable β	110	914	1033
Ti-15Mo-5Zr-3Al	Metastable β	82	771	812
Ti-13Nb-13Zr	α′+β	79	900	1030
Ti-35Nb-5Ta-7Zr	Metastable β	55	530	590

Titanium, with a melting point of 1678°C, undergoes an allotropic transformation , at 882°C [71]. In this study, the application of titanium alloy in the biomedical field was focused. The hcp (Hexagonal closed packed) α phase structure changed to bcc β phase structure. Mechanical properties of different titanium alloys are given in **Table 2-1**, showing change in mechanical properties with phase transformation.

A thermo-mechanical modeling approach for the additive manufacturing process of Ti-6Al-4V was presented where material properties were considered as a function of temperature and state of matter [72]. The microstructure of Ti-6Al-4V usually comprises of hexagonal close-packed (hcp) α-phase, body-centered cubic (bcc) β-phase, and

martensitic α′-phase. The transformation between these three phases was categorized as martensitic transformation and two diffusional transformations. These transformation models were defined as employing Koistinen-Marburger (KM) and Johnson-Mehl-Avrami (JMA) models, respectively. If the cooling rate, $\dot{T}$ is higher than $\dot{T}_{MT} = 410℃/s$, the martensitic transformation β→α′ occurs. Whereas Johnson-Mehl-Avrami (JMA) models were initially proposed for isothermal conditions and extended further for non-isothermal condition [72]. The solid phase transformation of Ti-6Al-4V is summarized in **Table 2-2**.

Table 2-2: Summery of solid phase transformation [72].

Transformation	Type	Occurring condition
β→α′	Martensitic	$\dot{T} < -\dot{T}_{MT} = -410℃/s$ (rapid cooling)
α′→α+β	Diffusional	$\dot{T} > 0$(heating)
β→α	Diffusional	$\dot{T} > -\dot{T}_{MT}$ (slow cooling or heating)

A combined computational and experimental approach was introduced to address correlation among process-structure-property-performance in the AM process [73]. A generic approach for metallurgical phase transformation for an arbitrary metal alloy was presented for predicting temperature evolution, residual stress, and distortion. Solid-phase transformation can simply be expressed as,

$$P_1 + P_2 + \ldots + P_{n_p} = C_1 + C_2 + \ldots + C_{n_c}. \quad \textbf{Eq. 2-7}$$

Here n_p and n_c denotes the number of parents and children phases, respectively. P_i and C_i are the i'th parent and child phase. A simplified transformation can be noted as P→C. The

volume fraction of master phases are given by, $f_p = \sum_{i=1}^{n_p} f_{P_i}$ and $f_c = \sum_{i=1}^{n_c} f_{c_i}$, respectively. Transformations can be diffusional or martensitic transformation. The diffusional transformation is expressed by the Johnson-Mehl-Avrami (JMA) model [74],

$$f_c = f_{tot}\left(1-e^{-kt^n}\right), \qquad \textbf{Eq. 2-8}$$

where $f_{tot} = f_c + f_p$, the total volume fraction of all children and parent phases; *k* and *n* are temperature-dependent coefficients. The values of these coefficients are calculated from the TTT diagram. **Figure 2-10** shows a sample of the TTT diagram of diffusional transformation (D) and martensitic transformation (M). Subscript s and f denote the starting curve and finishing curve, respectively.

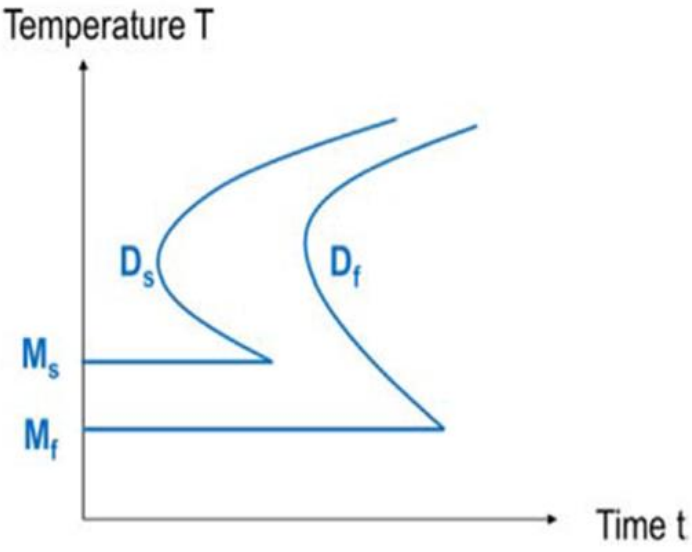

Figure 2-10: An example of a time-temperature-transformation (TTT) diagram [73].

The martensitic transformation is defined by the Koistinen-Marburger (KM) model [74], and only depends on the temperature,

$$f_c(T) = f_c(T_o) + (f_p(T_o) - f_{pr})[1 - exp - \gamma(M_s - T)]. \qquad \textbf{Eq. 2-9}$$

Here T_o is the temperature at the beginning of the cooling cycle, M_s is the martensitic temperature γ is the transformation coefficient. f_c and f_p are volume fraction of parent and child phase present in the alloy. $f_{pr} = 0.25 - 0.25 f_p$ [74]. The value of γ is calculated from the TTT diagram.

A thermomechanical microstructural model was developed based on the flow stress of Ti-6Al-4V and phase transformation kinetics. The α→β phase transformation was numerically investigated during heating and decomposition of the β phase [75]. During cooling, decomposition of β phase provides martensitic α′ or a secondary α phase. Following the previously mentioned Johnson–Mehl–Avrami (JMA) model for non-isothermal process, the phase transformation can be defined. Fabrication of Ni-rich NiTi alloy by means of wire arc additive manufacturing was studied [76]. Thermal history of the fabrication process affects the phase evolution. **Figure 2-11** shows differential scanning calorimetry (DSC) thermograms results that were carried out with DSC tester with heating and cooling rate of 10K/min. In **Figure 2-11** a, variation of heat flow vs. temperature lower, upper-middle, and upper regions is defined. At selected locations, characteristic transformation temperatures are shown in **Figure 2-11** b.

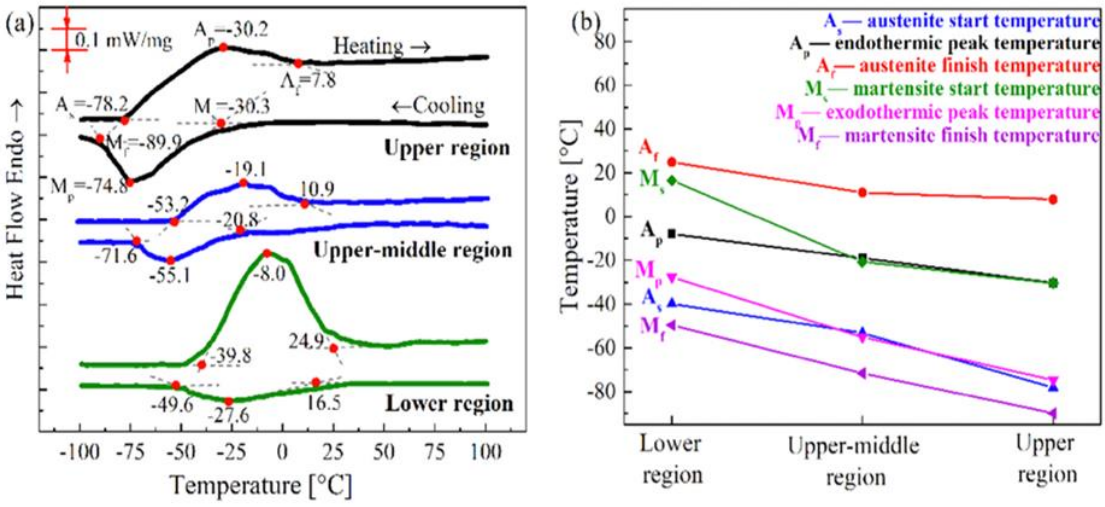

Figure 2-11: DSC experiments observations for forward and reverses martensitic phase transformation temperatures from different regions [76].

Phase transformation characteristics and mechanical properties of laser direct deposited from nickel and titanium powders were introduced [77]. Changing the ratio of Ni and Ti powder, various transformation temperature was achieved. A two-step transformation is shown in **Figure 2-12**. The cooling curve associated with the transformation of austenite to intermediate R-phase is shown in **Figure 2-12**a, and the cooling curve associated with the transformation of austenite to intermediate R-phase and transformation of intermediate R-phase to martensitic (partial) is shown in **Figure 2-12**b. Various researchers are working on the application of phase transformation via heat treatment to control residual stress in the additive manufacturing process.

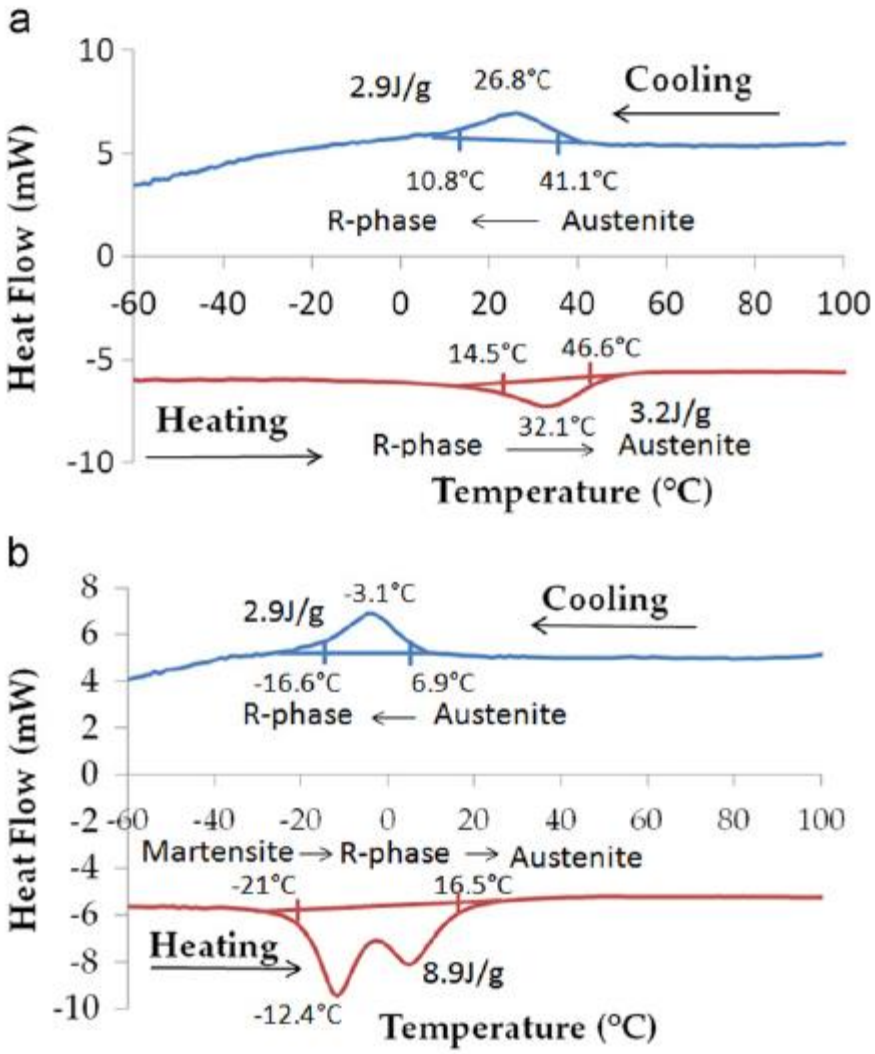

Figure 2-12: DSC plot for deposited from Ni and Ti powder mixture (1:1.33) after annealing at1050℃ for 10H and aged at (a) 400℃ for 1H and (b) 500℃ for 1H [77].

2.3 Computational approach

Temperature distribution and different cycles associated with various AM processes result in porosity and other microstructural discontinuities in fabricated parts. Thus, modeling of microstructure evolution during solidification is important to predict and control microstructural properties. To predict the evolution of AM fabricated microstructure; length and time scale solidification modeling is required. Different

computational approaches like phase field modeling, molecular dynamics simulations, finite element modeling, and Monte Carlo simulations are popular to study the microstructural evolution at the interface. The Monte carlo simulations only predicts the thermodynamic properties. Phase field simulations predicts both kinetics of phase transformation and thermodynamic properties. For the binary alloy, the phase field approach was applied.

CHAPTER 3

ALLOY PHASE FIELD MODEL

Phase field modeling is a popular approach to predict the composition and structure of the solidification microstructure at domain and interface. This model uses a set of field variables that are continuous along the interface region. Conserved and nonconserved are two types of field variables. These variables control the total free energy of an inhomogeneous microstructure system. By solving Ginzburg Landau (GL) and Cahn Hilliard with the total free energy the evolution of microstructure is predicted. The phase field approach is less expensive compare to other computational approaches. For mathematical modeling, we use the simplest expression for the Helmholtz free energy. The Helmholtz energy is expressed as,

$$\psi = \psi^{l} + \psi^{\nabla} = \psi^{\theta} + \breve{\psi}^{\theta} + \psi^{\nabla}, \qquad \textbf{Eq. 3-1}$$

Here ψ^{l} is the free energy and ψ^{∇} is the gradient energy. Free energy is expressed as the sum of thermal energy ψ^{θ} and the energy barrier $\breve{\psi}^{\theta}$. Thermal energy and the energy barrier are presented by **Eq. 3-2** and **Eq. 3-3**, respectively.

$$\psi^{\theta}(\theta, c, \Upsilon) = G_0^{\theta} + \Delta G_{S0}^{\theta}(\theta, c) q(\Upsilon, a), \qquad \textbf{Eq. 3-2}$$

$$\breve{\psi}^{\theta}(\theta, c, \Upsilon) = A^{S0}(\theta, c) \breve{q}(\Upsilon), \qquad \textbf{Eq. 3-3}$$

where G_0^{θ}, $\Delta G_{S0}^{\theta}(\theta, c)$ and $A^{S0}(\theta, c)$ is a function of temperature θ and concentration$c$; it depends on the material property. $G_0^{\theta} \equiv f^{L}(c_L)$ and $\Delta G_{S0}^{\theta}(\theta, c) = f^{S}(c_S) - f^{L}(c_L)$, is the free energy difference between solid and liquid. $f^{L}(c_L)$ and $f^{S}(c_S)$ are the free energy

densities of liquid and solid as function of composition. $A^{S0}(\theta, c)$ is the height of the double well potential. $q(\Upsilon, a)$ and $\breve{q}(\Upsilon)$ are expressed as,

$$q(\Upsilon, a) = a\Upsilon^2 - 2(a-2)\Upsilon^3 + (a-3)\Upsilon^4, \quad \textbf{Eq. 3-4}$$

$$\breve{q}(\Upsilon) = \Upsilon^2(1-\Upsilon)^2. \quad \textbf{Eq. 3-5}$$

From liquid to solid side Υ changed from 0 to 1, and a is a material property. The mole fraction c is expressed as,

$$c = (c_S^B - c_L^B)q(\Upsilon, a) + c_L^B, \quad \textbf{Eq. 3-6}$$

where, c_S^B and c_L^B are the compositions of bulk solid and bulk liquid. From **Eq. 3-2** and **Eq. 3-3** free energy is expressed as,

$$\begin{aligned} \psi^l = \psi^\theta + \breve{\psi}^\theta &= f(c, \Upsilon, \theta) \\ &= G_0^\theta + \Delta G_{S0}^\theta(\theta, c)q(\Upsilon, a) + A^{S0}(\theta, c)\breve{q}(\Upsilon). \end{aligned} \quad \textbf{Eq. 3-7}$$

For the phase field model we consider the first derivative of both free energies with respect to their concentration are equal,

$$f_{c_S}^S[c_S(x,t)] = f_{c_L}^L[c_L(x,t)]. \quad \textbf{Eq. 3-8}$$

Here subscript indicates derivatives of free energy. So, $f_{c_S}^S[c_S(x,t)] = df^S/dc_S$ and $f_{c_L}^L[c_L(x,t)] = df^L/dc_L$. Differentiating **Eq. 3-8** with respect to c_S and rearranging,

$$\left(\frac{\partial c_L}{\partial c_S}\right) = \frac{f_{cc}^S(c_S)}{f_{cc}^L(c_L)}. \quad \textbf{Eq. 3-9}$$

Here we used the notations of $f_{cc}^L(c_L) = d^2f^L/dc_L^2$ and $f_{cc}^S(c_L) = d^2f^S/dc_S^2$. Differentiating **Eq. 3-6** with respect to c_L, composition of liquid at the interface,

$$\frac{\partial c}{\partial c_L} = q(\Upsilon, a)\left(\frac{\partial c_S}{\partial c_L} - 1\right) + 1. \quad \textbf{Eq. 3-10}$$

Putting values from **Eq. 3-9**,

$$\frac{\partial c}{\partial c_L} = q(\Upsilon, a)\left(\frac{f_{cc}^{L}(c_L)}{f_{cc}^{S}(c_S)} - 1\right) + 1. \qquad \textbf{Eq. 3-11}$$

Rearranging **Eq. 3-11**,

$$\frac{\partial c_L}{\partial c} = \frac{f_{cc}^{S}(c_S)}{[1 - q(\Upsilon, a)]f_{cc}^{S}(c_S) + q(\Upsilon, a)f_{cc}^{L}(c_L)}. \qquad \textbf{Eq. 3-12}$$

Similarly, for the solid side,

$$\frac{\partial c_S}{\partial c} = \frac{f_{cc}^{L}(c_L)}{[1 - q(\Upsilon, a)]f_{cc}^{S}(c_S) + q(\Upsilon, a)f_{cc}^{L}(c_L)}. \qquad \textbf{Eq. 3-13}$$

Here c_S is the composition of solid at the interface. Differentiating **Eq. 3-6** with respect toΥ,

$$\frac{\partial c}{\partial \Upsilon} = (c_S^B - c_L^B)q'(\Upsilon, a). \qquad \textbf{Eq. 3-14}$$

Now applying chain rule and Putting value from **Eq. 3-12** and **Eq. 3-14**,

$$\frac{\partial c_L}{\partial \Upsilon} = \frac{(c_S^B - c_L^B)q'(\Upsilon, a)f_{cc}^{S}(c_S)}{[1 - q(\Upsilon, a)]f_{cc}^{S}(c_S) + q(\Upsilon, a)f_{cc}^{L}(c_L)}, \qquad \textbf{Eq. 3-15}$$

Similarly, for the solid side,

$$\frac{\partial c_S}{\partial \Upsilon} = \frac{(c_S^B - c_L^B)q'(\Upsilon, a)f_{cc}^{L}(c_L)}{[1 - q(\Upsilon, a)]f_{cc}^{S}(c_S) + q(\Upsilon, a)f_{cc}^{L}(c_L)}. \qquad \textbf{Eq. 3-16}$$

Now free energy,

$$\psi^l = G_0^\theta + \Delta G_{S0}^\theta(\theta, c)q(\Upsilon, a) + A^{S0}(\theta, c)\breve{q}(\Upsilon). \qquad \textbf{Eq. 3-17}$$

Differentiating with respect to Υ,

$$\psi^l{}_\Upsilon = \frac{\partial}{\partial \Upsilon}\left(G_0^\theta\right) + q'(\Upsilon, a)\Delta G_{S0}^\theta(\theta, c) + q(\Upsilon, a)\frac{\partial}{\partial \Upsilon}\left[\Delta G_{S0}^\theta(\theta, c)\right] + A^{S0}(\theta, c)\breve{q}'(\Upsilon) + \breve{q}(\Upsilon)\frac{\partial A^{S0}(\theta, c)}{\partial \Upsilon}. \qquad \textbf{Eq. 3-18}$$

Now, Putting the values from **Eq. 3-15** and **Eq. 3-16**,

$$\frac{\partial}{\partial \Upsilon}\left[\Delta G_{S0}^{\theta}(\theta,c)\right]=\frac{\partial}{\partial \Upsilon}[f^{S}(c_S)-f^{L}(c_L)]=\frac{\partial}{\partial \Upsilon}[f^{S}(c_S)]-\frac{\partial}{\partial \Upsilon}[f^{L}(c_L)]$$

$$=\left(\frac{\partial f^{S}(c_S)}{\partial c_S}\right)\frac{\partial c_S}{\partial \Upsilon}-\left(\frac{\partial f^{L}(c_L)}{\partial c_L}\right)\frac{\partial c_L}{\partial \Upsilon},$$

$$\Rightarrow \frac{\partial}{\partial \Upsilon}\left[\Delta G_{S0}^{\theta}(\theta,c)\right]=\frac{q'(\Upsilon,a)\frac{\partial f^{L}(c_L)}{\partial c_L}(c_S^{B}-c_L^{B})[f_{cc}^{L}(c_L)-f_{cc}^{S}(c_S)]}{[1-q(\Upsilon,a)]f_{cc}^{S}(c_S)+q(\Upsilon,a)f_{cc}^{L}(c_L)}.$$

Again, for $\frac{\partial}{\partial \Upsilon}\left(G_0^{\theta}(c_{L)}\right)$ we have,

$$\frac{\partial}{\partial \Upsilon}\left(G_0^{\theta}(c_L)\right)=\frac{\partial}{\partial \Upsilon}\left(f^{L}(c_L)\right)=\left(\frac{\partial f^{L}(c_L)}{\partial c_L}\right)\frac{\partial c_L}{\partial \Upsilon}$$

$$=\frac{\partial f^{L}(c_L)}{\partial c_L}\frac{(c_S^{B}-c_L^{B})q'(\Upsilon,a)f_{cc}^{S}(c_S)}{[1-q(\Upsilon,a)]f_{cc}^{S}(c_S)+q(\Upsilon,a)f_{cc}^{L}(c_L)}.$$

Now putting the values of $\frac{\partial}{\partial \Upsilon}\left[\Delta G_{S0}^{\theta}(\theta,c)\right]$ and $\frac{\partial}{\partial \Upsilon}\left(G_0^{\theta}\right)$ in **Eq. 3-18**

$$\psi^{l}{}_{\Upsilon}$$

$$=q'(\Upsilon,a)\Delta G_{S0}^{\theta}(\theta,c)$$

$$+\frac{\partial f^{L}(c_L)}{\partial c_L}\frac{(c_S^{B}-c_L^{B})q'(\Upsilon,a)f_{cc}^{S}(c_S)}{[1-q(\Upsilon,a)]f_{cc}^{S}(c_S)+q(\Upsilon,a)f_{cc}^{L}(c_L)}$$

$$+q(\Upsilon,a)\left[\frac{q'(\Upsilon,a)\frac{\partial f^{L}(c_L)}{\partial c_L}(c_S^{B}-c_L^{B})[f_{cc}^{S}(c_S)-f_{cc}^{L}(c_L)]}{[1-q(\Upsilon,a)]f_{cc}^{S}(c_S)+q(\Upsilon,a)f_{cc}^{L}(c_L)}\right] \qquad \textbf{Eq. 3-19}$$

$$+A^{S0}(\theta,c)\breve{q}'(\Upsilon)+\breve{q}(\Upsilon)\frac{\partial A^{S0}(\theta,c)}{\partial c}\frac{\partial c}{\partial \Upsilon}$$

$$\Rightarrow \psi^{l}{}_{\Upsilon}=q'(\Upsilon,a)\left[\Delta G_{S0}^{\theta}(\theta,c)+\frac{\partial f^{L}(c_L)}{\partial c_L}(c_S^{B}-c_L^{B})\right]$$

$$+A^{S0}(\theta,c)\breve{q}'(\Upsilon)+\breve{q}(\Upsilon)\frac{\partial A^{S0}(\theta,c)}{\partial c}(c_S^{B}-c_L^{B})q'(\Upsilon,a)$$

Now gradient energy is expressed as [78],

$$\psi^{\nabla} = 0.5\ (\beta^{S0}\nabla\Upsilon^2). \qquad \textbf{Eq. 3-20}$$

Here, β^{S0} is the gradient energy coefficient. This is the lowes degree potential function granting a linear relation between the thermodynamic driving force and $\nabla\Upsilon$. Now, differentiating **Eq. 3-20** with respect to Υ,

$$\psi^{\nabla}{}_{\Upsilon} = \nabla.[\beta^{S0}\nabla\Upsilon]. \qquad \textbf{Eq. 3-21}$$

Putting the value of free energy and gradient energy in **Eq. 3-1**

$$\psi = \Delta G^{\theta}_{S0}(\theta, c)q(\Upsilon, a) + A^{S0}(\theta, c)\breve{q}(\Upsilon) + \nabla.[\beta^{S0}\nabla\Upsilon]. \qquad \textbf{Eq. 3-22}$$

Differentiating with respect to Υ and putting the values,

$$\begin{aligned}\psi_{\Upsilon} = q'(\Upsilon, a)&\left[\Delta G^{\theta}_{S0}(\theta, c) + \frac{\partial f^{L}(c_L)}{\partial c_L}(c^{B}_{S} - c^{B}_{L})\right] \\ &+ A^{S0}(\theta, c)\breve{q}'(\Upsilon) \\ &+ \breve{q}(\Upsilon)\frac{\partial A^{S0}(\theta, c)}{\partial c}(c^{B}_{S} - c^{B}_{L})\breve{q}'(\Upsilon) + \nabla.[\beta^{S0}\nabla\Upsilon].\end{aligned} \qquad \textbf{Eq. 3-23}$$

Now from GL Equation,

$$\frac{1}{L_{\Upsilon}}\frac{\partial\Upsilon}{\partial t} = -\frac{\partial\psi^{l}}{\partial\Upsilon} + \nabla.[\beta^{S0}\nabla\Upsilon]. \qquad \textbf{Eq. 3-24}$$

For simplicity let us assume $A^{S0}(\theta, c)$ is constant. So $\frac{\partial A^{S0}(\theta,c)}{\partial c} = 0$. Putting the value from **Eq. 3-19**

$$\begin{aligned}\frac{1}{L_{\Upsilon}}\frac{\partial\Upsilon}{\partial t} = -\Bigg\{&q'(\Upsilon, a)\left[\Delta G^{\theta}_{S0}(\theta, c) + \frac{\partial f^{L}(c_L)}{\partial c_L}(c^{B}_{S} - c^{B}_{L})\right] \\ &+ A^{S0}(\theta, c)\breve{q}'(\Upsilon)\Bigg\} + \nabla.[\beta^{S0}\nabla\Upsilon].\end{aligned} \qquad \textbf{Eq. 3-25}$$

Now differentiating **Eq. 3-17** with respect to c,

$$\psi^{l}{}_{c} = q(\Upsilon, a)\left(\frac{d}{dc}\left[\Delta G^{\theta}_{S0}(\theta, c)\right]\right) + \frac{\partial}{\partial c}\left(G^{\theta}_{0}\right) + \breve{q}(\Upsilon)\frac{dA^{S0}(\theta, c)}{dc}$$

$$= q(\Upsilon, a)\left[\frac{d}{dc}[f^S(c_S)] - \frac{d}{dc}[f^L(c_L)]\right] + \frac{d}{dc}[f^L(c_L)] + \breve{q}(\Upsilon)\frac{dA^{S0}(\theta, c)}{dc}$$

$$= q(\Upsilon, a)\left[\left(\frac{\partial f^S(c_S)}{\partial c_L}\right)\frac{\partial c_S}{\partial c} - \left(\frac{\partial f^L(c_L)}{\partial c_L}\right)\frac{\partial c_L}{\partial c}\right] + \left(\frac{\partial f^L(c_L)}{\partial c_L}\right)\frac{\partial c_L}{\partial c}$$

$$+ \breve{q}(\Upsilon)\frac{dA^{S0}(\theta, c)}{dc} \qquad \textbf{Eq. 3-26}$$

$$= \left(\frac{\partial f^L(c_L)}{\partial c_L}\right)\left[q(\Upsilon, a)\left(\frac{\partial c_S}{\partial c} - \frac{\partial c_L}{\partial c}\right) + \frac{\partial c_L}{\partial c}\right] + \breve{q}(\Upsilon)\frac{dA^{S0}(\theta, c)}{dc}.$$

Putting values from **Eq. 3-12** and **Eq. 3-13**,

$$\psi^l{}_c = \frac{\partial f^L(c_L)}{\partial c_L} + \breve{q}(\Upsilon)\frac{dA^{S0}(\theta, c)}{dc}. \qquad \textbf{Eq. 3-27}$$

Differentiating **Eq. 3-26** with respect to c,

$$\psi^l{}_{cc} = \frac{f^L_{cc}(c_L) f^S_{cc}(c_S)}{[1 - q(\Upsilon, a)]f^S_{cc}(c_S) + q(\Upsilon, a)f^L_{cc}(c_L)} + \breve{q}(\Upsilon)\frac{d^2A^{S0}(\theta, c)}{dc^2}. \qquad \textbf{Eq. 3-28}$$

Differentiating $\psi^l{}_c$ with respect to Υ,

$$\psi^l{}_{c\Upsilon} = \frac{d}{d\Upsilon}\left[\frac{df^L(c_L)}{dc_L}\right] + \frac{dA^{S0}(\theta, c)}{dc}\breve{q}'(\Upsilon)$$

$$= \frac{d^2f^L(c_L)}{dc_L{}^2}\frac{\partial c_L}{\partial \Upsilon} + \frac{dA^{S0}(\theta, c)}{dc}\breve{q}'(\Upsilon) \qquad \textbf{Eq. 3-29}$$

$$= \frac{(c_S^B - c_L^B)q'(\Upsilon, a)f^S_{cc}(c_S)f^L_{cc}(c_L)}{[1 - q(\Upsilon, a)]f^S_{cc}(c_S) + q(\Upsilon, a)f^L_{cc}(c_L)} + \frac{dA^{S0}(\theta, c)}{dc}\breve{q}'(\Upsilon).$$

The Cahn-Hilliard equation is expressed as,

$$c_t = \nabla.\frac{D(\Upsilon)}{\psi^l{}_{cc}}\nabla\psi^l{}_c. \qquad \textbf{Eq. 3-30}$$

Here $D(\Upsilon)$ is the diffusivity. Diffusivity depends on phase field. Putting the value of $\psi^{l}{}_{c}$ from **Eq. 3-26**,

$$\frac{\partial c}{\partial t} = \nabla\left[\frac{D(\Upsilon)}{\psi^{l}{}_{cc}}\nabla\left\{\frac{df^{L}(c_L)}{dc_L} + \breve{q}(\Upsilon)\frac{dA^{S0}(\theta, c)}{dc}\right\}\right]. \qquad \textbf{Eq. 3-31}$$

Eq. 3-25 and **Eq. 3-31** are the basic equation for binary alloy model.

CHAPTER 4

DILUTE SOLUTION APPROXIMATION

The dilute solution limit is frequently applicable for both engineering applications and to understand the fundamental science governing the phase transformation. Let us consider a binary alloy of A and B. The chemical potential of A and B can approximately be represented as follows,[79]

$$\mu_A^L = \mu_A^{oL} + RTln(1-c);\ \ \mu_A^S = \mu_A^{oS} + RTln(1-c);$$
$$\mu_B^L = \mu_B^{oL} + RTln(\gamma^L c);\ \ \mu_B^S = \mu_B^{oS} + RTln(\gamma^S c). \qquad \textbf{Eq. 4-1}$$

Here R is the gas constant, and T is the temperature of the isothermal system. γ^S and γ^L are the activity coefficients of solid and liquid phases, respectively. At equilibrium condition, $\mu_A^L = \mu_A^S$ and $\mu_B^L = \mu_B^S$. Applying this relation of the thermochemical potential at equilibrium concentration and setting liquid phase as a standard state, we can rewrite **Eq. 4-1** as,

$$\mu_A^{oL} = 0;\ \ \mu_B^{oL} = 0. \qquad \textbf{Eq. 4-2}$$

Now,

$$\mu_A^L = \mu_A^S \Rightarrow \mu_A^{oL} + RTln(1 - c_L^e) = \mu_A^{oS} + RTln(1 - c_S^e) \Rightarrow \mu_A^{oS}$$

$$= RTln\left(\frac{1 - c_L^e}{1 - c_S^e}\right),$$

$$\mu_B^L = \mu_B^S \Rightarrow \mu_B^{oL} + RTln(\gamma^L c_L^e) = \mu_B^{oS} + RTln(\gamma^S c_S^e) \Rightarrow \mu_B^{oS} \quad \textbf{Eq. 4-3}$$

$$= RTln\left(\frac{c_L^e}{c_S^e}\right) + RTln\left(\frac{\gamma^L}{\gamma^S}\right).$$

Here c_L^e and c_S^e are the equilibrium concentration of the liquid side and solid side, respectively. We can set $\gamma^L = \gamma^S = 1$. As these values do not affect the equilibrium state and the driving force for the transformation. These relations are used to derive the free energy density of solid and liquid. Now, the following form of the free energy density for liquid phase is used [79],

$$f^L(c_L)$$

$$= \frac{[(1 - c_L)\mu_A^{oL} + c_L\mu_B^{oL} + RT\{c_L lnc_L + (1 - c_L) l\, n(1 - c_L)\}]}{V_m}, \quad \textbf{Eq. 4-4}$$

$$\Rightarrow f^L(c_L) = \frac{RT}{V_m}[c_L lnc_L + (1 - c_L)\, ln(1 - c_L)].$$

Differentiating **Eq. 4-4** with respect to c_L,

$$f_{c_L}^L(c_L) = \frac{RT}{V_m} ln\left(\frac{c_L}{1 - c_L}\right). \quad \textbf{Eq. 4-5}$$

Again, differentiating **Eq. 4-5** with respect to c_L,

$$f_{cc}^L(c_L) = \frac{RT}{V_m}\frac{1}{(1 - c_L)c_L}. \quad \textbf{Eq. 4-6}$$

Now the free energy density for solid phase [79],

$$f^S(c_S)$$

$$= \frac{[(1-c_S)\mu_A^{oS} + c_S\mu_B^{oS} + RT\{c_S lnc_S + (1-c_S)l\,n(1-c_S)\}]}{V_m},$$

$$\Rightarrow f^S(c_S) = \frac{RT}{V_m}\left[(1-c_S)ln\left(\frac{1-c_L^e}{1-c_S^e}\right) + c_S RT ln\left(\frac{c_L^e}{c_S^e}\right)\right. \quad \textbf{Eq. 4-7}$$

$$\left. + c_S lnc_S + (1-c_S)ln\,(1-c_S)\right].$$

Here, V_m is the molar volume and R is the molar gas constant. Differentiating **Eq. 4-7** with respect to c_S,

$$f_{c_S}^S(c_S) = \frac{RT}{V_m} ln\left(\frac{c_S}{1-c_S}\right). \quad \textbf{Eq. 4-8}$$

Again differentiating **Eq. 4-8** with respect to c_S,

$$f_{cc}^S(c_S) = \frac{RT}{V_m}\frac{1}{(1-c_S)c_S}. \quad \textbf{Eq. 4-9}$$

Putting the value from **Eq. 4-5** and **Eq. 4-8** in **Eq. 3-8** and reorganizing,

$$\frac{c_L}{1-c_L} = \frac{c_S}{1-c_S},$$

$$\Rightarrow \frac{c_L}{c_S} = \frac{1-c_L}{1-c_S}, \quad \textbf{Eq. 4-10}$$

$$\Rightarrow c_L = c_S.$$

From **Eq. 4-10**, similarly for equilibrium condition,

$$\frac{c_S^e}{c_L^e} = \frac{1-c_S^e}{1-c_L^e}, \quad \textbf{Eq. 4-11}$$

Multiplying **Eq. 4-10** and **Eq. 4-11**,

$$\frac{c_S^e c_L}{c_L^e c_S} = \frac{(1-c_S^e)(1-c_L)}{(1-c_L^e)(1-c_S)}. \quad \textbf{Eq. 4-12}$$

Now,

$$G(c_S, c_L) \equiv \Delta G_{S0}^{\theta}(\theta, c) + \frac{df^L(c_L)}{dc_L}(c_S^B - c_L^B) = f^L(c_L) - f^S(c_S) - (c_L - c_S) f_{c_L}^L(c_L). \quad \textbf{Eq. 4-13}$$

Putting the value from **Eq. 4-4**, **Eq. 4-5** and **Eq. 4-7**,

$$G(c_S, c_L) = \frac{RT}{V_m} ln \frac{(1 - c_S^e)(1 - c_L^B)}{(1 - c_L^e)(1 - c_S^B)}. \quad \textbf{Eq. 4-14}$$

Now applying Tylor's expansion avoiding higher-order term,

$$G(c_S, c_L) = \frac{RT}{V_m}[(c_L^e - c_S^e) - (c_L - c_S)]. \quad \textbf{Eq. 4-15}$$

At limit where all compositions go to zero **Eq. 4-11** can further be approximated as

$$\frac{c_S}{c_L} = \frac{c_S^e}{c_L^e} = k^e. \quad \textbf{Eq. 4-16}$$

Here k^e is the equilibrium coefficient. Now putting $c_S = k^e c_L$ and $c_S^e = k^e c_L^e$ in **Eq. 4-15** from **Eq. 4-16** we can derive that,

$$G(c_S, c_L) = \frac{RT}{V_m}[(c_L^e - k^e c_L^e) - (c_L - k^e c_L)] = \frac{RT}{V_m}\frac{1 - k^e}{m^e}(m^e c_L^e - m^e c_L), \quad \textbf{Eq. 4-17}$$

where m^e is the liquids slope in phase diagram. Now, for the dilute solution,[80]

$$T = T_m - m^e c_L \left(1 + \frac{(k^e - k) + k ln\left({}^{k}/_{k^e}\right)}{1 - k^e}\right) - \frac{V_n}{RT}\frac{\alpha m^e}{1 - k^e} v_n. \quad \textbf{Eq. 4-18}$$

Here v_n is the interface velocity. $k = c_S/c_L$ For equilibrium condition, $k^e = k$ and interface velocity, $v_n = 0$. T is the temperature of the isothermal system. T_m is the melting temperature of pure solvent. So, **Eq. 4-18** is reduced to,

$$T = T_m - m^e c_L^e. \quad \textbf{Eq. 4-19}$$

So, from **Eq. 4-17**,

$$G(c_S, c_L) = \frac{RT}{V_m}\frac{1-k^e}{m^e}(T_m - T - m^e c_L). \qquad \textbf{Eq. 4-20}$$

Now from **Eq. 3-25**,

$$\frac{1}{L_\Upsilon}\frac{\partial \Upsilon}{\partial t} = -\{q'(\Upsilon, a)G(c_S, c_L) + A^{S0}(\theta, c)\breve{q}'(\Upsilon)\} + \breve{q}(\Upsilon)\frac{\partial A^{S0}(\theta, c)}{\partial \Upsilon} + \nabla.[\beta^{S0}\nabla\Upsilon]. \qquad \textbf{Eq. 4-21}$$

Putting the value from **Eq. 4-20**,

$$\frac{1}{L_\Upsilon}\frac{\partial \Upsilon}{\partial t} = -\left\{q'(\Upsilon, a)\frac{RT}{V_m}\frac{1-k^e}{m^e}(T_m - T - m^e c_L) + A^{S0}(\theta, c)\breve{q}'(\Upsilon)\right\} + \nabla.[\beta^{S0}\nabla\Upsilon]. \qquad \textbf{Eq. 4-22}$$

For a dilute solution, the height of double-well potential is constant. Putting the value of **Eq. 4-6** and **Eq. 4-9**, in **Eq. 3-28**,

$$\psi^{l}{}_{cc} = \frac{RT}{V_m}\frac{1}{\big(1-q(\Upsilon, a)\big)(1-c_L)c_L + q(\Upsilon, a)(1-c_S)c_S}. \qquad \textbf{Eq. 4-23}$$

So,

$$H(\Upsilon, c_S, c_L) \equiv \frac{RT}{V_m \psi^{l}{}_{cc}} = \big(1-q(\Upsilon, a)\big)(1-c_L)c_L + q(\Upsilon, a)(1-c_S)c_S. \qquad \textbf{Eq. 4-24}$$

Now putting the value of **Eq. 4-5** and **Eq. 4-24** in **Eq. 3-31**

$$\frac{\partial c}{\partial t} = \nabla\left[D(\Upsilon)H(\Upsilon, c_S, c_L)\nabla ln\left(\frac{c_L}{1-c_L}\right)\right]. \qquad \textbf{Eq. 4-25}$$

In summary, we derived both Ginzburg Landau equation and Cahn Hilliard equations for the dilute solution approximation, i.e., **Eq. 4-22** and **Eq. 4-25**, respectively.

CHAPTER 5

ANALYTICAL SOLUTION OF GINZBURG-LANDAU EQUATION

In this chapter, we will derive the analytical solution for Ginzburg Landau equation. Then we will plot the free energy of solid and liquid side with common tangent line. From **Eq. 3-4**, **Eq. 3-5** and **Eq. 3-7** free energy is expressed as,

$$\psi^l = G_0^\theta + \Delta G_{S0}^\theta(\theta, c)[a\Upsilon^2 - 2(a-2)\Upsilon^3 + (a-3)\Upsilon^4] + A^{S0}(\theta, c)[\Upsilon^2(1-\Upsilon)^2]. \quad \textbf{Eq. 5-1}$$

Reorganizing **Eq. 5-1** and putting $a = 0$ and $G_0^\theta = 0$, we have

$$\psi^l = A^{S0}(\theta, c)\Upsilon^2\left[1 - \frac{(6-P)\Upsilon}{3} + \frac{(4-P)\Upsilon^2}{4}\right]. \quad \textbf{Eq. 5-2}$$

Here,

$$P(\theta, c) = \frac{12\Delta G_{S0}^\theta(\theta, c)}{A^{S0}(\theta, c)}. \quad \textbf{Eq. 5-3}$$

Differentiating **Eq. 5-2** with respect to Υ,

$$\frac{\partial \psi^l}{\partial \Upsilon} = A^{S0}(\theta, c)\Upsilon(1-\Upsilon)[2-(4-P)\Upsilon]. \quad \textbf{Eq. 5-4}$$

Now we calculate the maxima ,

$$\frac{\partial^2 \psi^l(0)}{\partial \Upsilon^2} = A^{S0}(\theta, c), \frac{\partial^2 \psi^l(1)}{\partial \Upsilon^2} = 2A^{S0}(\theta, c)(2-P)$$
$$\Upsilon_3 = \frac{2}{4-p}, \quad \psi_3^l = \frac{\partial^2 \psi^l(\Upsilon_3)}{\partial \Upsilon^2} = \frac{4}{3}\frac{A^{S0}(\theta, c)(3-P)}{(4-P)^3}, \quad \textbf{Eq. 5-5}$$

where Υ_3 are the maxima of ψ^l. The Ginzburg-Landau energy, $\psi = \psi^l + (\beta^{S0}|\nabla\Upsilon|^2)$. Here β^{S0} is a linear combination of components of the second–rank tensor β^{S0} in the crystal coordinates. This energy leads to time-dependent Ginzburg-Landau equation,

$$\frac{\partial \Upsilon}{\partial t} = -\lambda \frac{\partial \psi}{\partial \Upsilon} = -\lambda \left(\frac{\partial \psi^l}{\partial \Upsilon} - 2\beta^{S0} \frac{\partial^2 \Upsilon}{\partial x^2} \right). \qquad \textbf{Eq. 5-6}$$

Here $\lambda > 0$ is the kinetic coefficient. Now we rescale **Eq. 5-6** in dimensionless form. The dimensionless potentials and order parameters are,

$$g = m\psi^l = B\xi^2 - \xi^3 + \xi^4, \quad \xi = k\Upsilon, \qquad \textbf{Eq. 5-7}$$

The parameter is defined and related as follows,

$$B = \frac{9(4-P)}{4(6-P)^2}, \quad k = \frac{3(4-P)}{4(6-P)}, m = \frac{81(4-P)^3}{A^{S0}(\theta,c)(6-P)^4} = \frac{k^2 B}{A^{S0}(\theta,c)}, \qquad \textbf{Eq. 5-8}$$

Here, *k* can be determined by the condition $\frac{\partial g}{\partial \xi} = 0$. Now we define ξ_1 and ξ_2,

$$\begin{aligned} g &= \xi^2(\xi - \xi_1)(\xi - \xi_2), \\ \xi_1 &= .5\left(1 - \sqrt{1 - 4B}\right), \\ \xi_2 &= .5\left(1 + \sqrt{1 - 4B}\right). \end{aligned} \qquad \textbf{Eq. 5-9}$$

Introducing new spatial and time variables by the equations,

$$y = \frac{k}{\sqrt{\beta^{S0} m}} x = \sqrt{\frac{A^{S0}(\theta,c)}{\beta^{S0} B}} x = \frac{2}{3\sqrt{\frac{A^{S0}(\theta,c)}{\beta^{S0}}} \frac{4-P}{\sqrt{6-P}} x}, \qquad \textbf{Eq. 5-10}$$

$$z = \frac{\lambda k^2}{m} t.$$

We obtain the dimensionless form of Ginzburg-Landau equation,

$$\frac{\partial \xi}{\partial z} = -\left(\frac{\partial g}{\partial \xi} - 2\frac{\partial^2 \xi}{\partial y^2} \right). \qquad \textbf{Eq. 5-11}$$

We only consider time-independent solution so, $\frac{\partial \Upsilon}{\partial z} = 0$. The resulting equation,

$$\frac{\partial g}{\partial \xi} = 2\frac{\partial^2 \xi}{\partial y^2}. \qquad \textbf{Eq. 5-12}$$

Eq. 5-12 is the equation of motion of material point with a mass equal to 2 in the potential field. An energy integral read,

$$\frac{d\xi}{dy} = \sqrt{g - g_0}, \qquad \textbf{Eq. 5-13}$$

where g_0 is an integral constant. At points $\frac{d\xi}{dy} = 0$, at the center of nucleus $g = g_0$. So,

$$g^*_{GL} = g_{GL} - g_o = g - g_0 + \left(\frac{d\xi}{dy}\right)^2 = 2(g - g_0). \qquad \textbf{Eq. 5-14}$$

Eq. 5-12 has a periodic solution with *n* diffuse interface. The total energy per unit area of *n* diffuse interface is given by,

$$e \coloneqq \int_{-l}^{l} g^*_{GL} dy = 2n \int_{-l}^{l} \sqrt{g - g_0}\, d\xi. \qquad \textbf{Eq. 5-15}$$

Here $l \coloneqq \sqrt{\frac{A^{S0}(\theta,c)}{\beta^{S0}B}} L$, $2L$ is the length of a parallelepiped in the x-direction. The energy *e*is finite even for an infinite slab. Imposing the boundary conditions at the end of the slab,

$$\frac{d\xi(-l)}{dy} = \frac{d\xi(l)}{dy} = 0, \qquad \textbf{Eq. 5-16}$$

$$g(-l) = g(l) = g_o. \qquad \textbf{Eq. 5-17}$$

Using **Eq. 5-7** and **Eq. 5-13**,

$$y(\xi) = \int \frac{d\xi}{\sqrt{(B\xi^2 - \xi^3 + \xi^4 - g_o)}}. \qquad \textbf{Eq. 5-18}$$

Now we consider $g(-\infty) = \mathrm{g}(\infty) = 0$, we find $P = 0, B = \frac{1}{4}$, $\xi_1 = \xi_2 = \frac{1}{2}$. $g = \xi^2(\xi - \frac{1}{2})^2$. The solution of **Eq. 3-15** [81],

$$\xi(y) = \left[2 + \left(1 + e^{-\frac{y-y_o}{2}}\right)\right]^{-1}, \qquad \textbf{Eq. 5-19}$$

$$\Upsilon(x) = \left[1 + e^{-\sqrt{\frac{A^{S0}(\theta,c)}{\beta^{S0}}}(x-x_o)}\right]^{-1}. \qquad \textbf{Eq. 5-20}$$

The solution is symmetric around $x = x_o$. The interface energy is given by [81],

$$E = \left(\frac{4}{3}\right)\sqrt{\beta^{S0}\psi_3^l}; \qquad \textbf{Eq. 5-21}$$

The interface thickness [81],

$$\Delta = p\sqrt{\beta^{S0}/\psi_3^l}; \qquad 2.411 \le P \le 2.667, \qquad \textbf{Eq. 5-22}$$

To plot the common tangent line of free energies, let the free energy of liquid and solid be represented by the sample following equations,

$$f^L(c_L) = y = 5(x-7)^4 + 30. \qquad \textbf{Eq. 5-23}$$

$$f^S(c_S) = y = 2(x-3)^4 + 10. \qquad \textbf{Eq. 5-24}$$

Figure 5-1 shows the free energy curves of solid and liquid. Q is the common tangent line. Now let us consider $x_1 \equiv c_L$ and $x_2 \equiv c_S$. Within the interface region, the composition of free energy density is represented as,

$$\psi = f^S(c_S) + [f^L(c_L) - f^S(c_S)]q(\Upsilon) + A^{S0}(\theta,c)\breve{q}(\Upsilon). \qquad \textbf{Eq. 5-25}$$

Here,

$$q(\Upsilon) = 4\Upsilon^3 - 3\Upsilon^4; \quad \breve{q}(\Upsilon) = \Upsilon^2(1-\Upsilon)^2 \; and \; \Upsilon = \frac{c - c_S}{c_L - c_S}. \qquad \textbf{Eq. 5-26}$$

The ψ is represented by the curve (P) in **Figure 5-1**. The height of the double-well potential, $A^{S0}(\theta,c)$ is considered a constant. As the height goes to zero, the curve passes through the intersecting point of **Eq. 5-23** and **Eq. 5-24**.

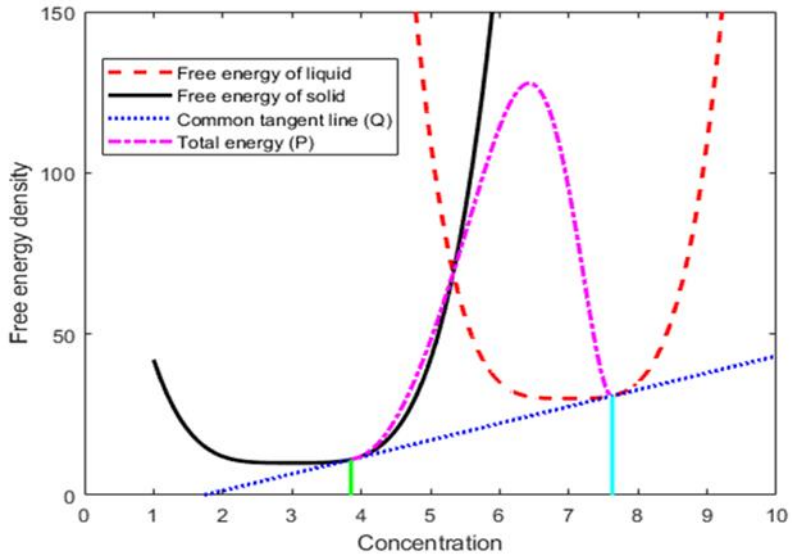

Figure 5-1: Free energy density curves of solid and liquid against composition.

CHAPTER 6

THIN INTERFACE LIMIT

In this section, for thin interface limit condition, where the interface thickness is small compared to the diffusive boundary layer, under an assumption of negligible diffusivity in solid at 1D instantaneous steady-state and $A^{S0}(\theta, c)$ is considered as constant **Eq. 3-25** and **Eq. 3-31** becomes,

$$-\frac{V}{L_\Upsilon}\frac{\partial \Upsilon}{\partial x} = -\left\{q'(\Upsilon, a)\left[\Delta G^{\theta}_{S0}(\theta, c) + \frac{df^L(c_L)}{dc_L}(c_S^B - c_L^B)\right] + A^{S0}(\theta, c)\breve{q}'(\Upsilon)\right\} + \beta^{S0}\frac{d^2\Upsilon}{dx^2}, \quad \textbf{Eq. 6-1}$$

$$-V\frac{\partial c}{\partial x} = \frac{d}{dx}\left[\frac{D(\Upsilon)}{\psi^l{}_{cc}}\frac{d}{dx}\frac{df^L(c_L)}{dc_L}\right]. \quad \textbf{Eq. 6-2}$$

Here, V is the interface velocity. Integrating **Eq. 6-2**,

$$Vc(x) + \frac{D(\Upsilon)}{\psi^l{}_{cc}}\frac{d}{dx}\frac{df^L(c_L)}{dc_L} = A. \quad \textbf{Eq. 6-3}$$

A is an integration constant. In liquid side **Eq. 6-3** gives,

$$\frac{D(\Upsilon)}{\psi^l{}_{\mathrm{cc}}}\frac{\mathrm{d}}{\mathrm{dx}}\frac{df^L(c_L)}{dc_L} = A - Vc_L,$$

$$\Rightarrow \frac{D(\Upsilon)}{\psi^l{}_{cc}}\psi^l{}_{cc}\frac{dc_L}{dx} = A - Vc_{L,}$$

$$\Rightarrow D_L(\Upsilon)\frac{dc_L}{dx} = A - Vc_L. \quad \textbf{Eq. 6-4}$$

Similarly, for the solid side, we can derive that,

$$D_S(\Upsilon)\frac{dc_S}{dx} = A - Vc_S. \qquad \textbf{Eq. 6-5}$$

As $D_S(\Upsilon)$ is considered as negligible. So,

$$A = Vc_S, \qquad \textbf{Eq. 6-6}$$

Putting the value of A in **Eq. 6-3** and Integrating, we get the potential chemical profile [80],

$$f_c(x) = f_c^S(c_S) - V\int_{-\infty}^{x}\frac{\psi^l{}_{cc}}{D(\Upsilon)}[c(x) - c_S]dx, \qquad \textbf{Eq. 6-7}$$

Here, $f_c^S(c_S)$ is the integration constant. $f_c^S(c_S)$ is the chemical potential of the solid phase. To calculate the chemical potential of liquid, we assume that the thermodynamic partitioning of concentration at the interface occurs sufficiently over the width of $-\lambda < x < \lambda$. Thus, the chemical potential of liquid then given by,

$$f_c^L(c_L) = f_c^S(c_S) - V\int_{-\lambda}^{\lambda}\frac{\psi^l{}_{cc}}{D(\Upsilon)}[c(x) - c_S]dx, \qquad \textbf{Eq. 6-8}$$

At interface c_S^i is the composition at the solid side ($x = -\lambda$) of the interface. So, the chemical potential's profile across the interface is given by,

$$f_c^L(c_L) = f_c^S\left(c_S^i\right) - V\int_{-\lambda}^{\lambda}\frac{\psi^l{}_{cc}}{D(\Upsilon)}\left[c(x) - c_S^i\right]dx, \qquad \textbf{Eq. 6-9}$$

Peclet number, $P = 2\lambda V/\widetilde{D}$ ($\widetilde{D}$ is average interface diffusivity). For equilibrium condition,

$$\Delta G_{S0}^{\theta}(\theta, c) + f_c^L(c_L)(c_S^B - c_L^B) = \Delta G_{S0}^{\theta}(\theta, c^e) - (c_L^e - c_S^e)f_{c_L}^L(c_L), \qquad \textbf{Eq. 6-10}$$

and,

$$\psi^l{}_{cc} = \psi^l{}_{cc}{}^e, \qquad \textbf{Eq. 6-11}$$

Now multiplying **Eq. 6-1** with $d\Upsilon/dx$ and integrating from $-\lambda$ to λ gives,

$$\frac{V}{L_\Upsilon}\int_{-\lambda}^{\lambda}\left(\frac{d\Upsilon}{dx}\right)^2 dx$$

$$= -\beta^{S0}\int_{-\lambda}^{\lambda}\frac{d^2\Upsilon}{dx^2}\frac{d\Upsilon}{dx}dx$$

$$+\int_{-\lambda}^{\lambda}\left(q'(\Upsilon,a)\left[\Delta G_{S0}^{\theta}(\theta,c^e)-(c_L^e\right.\right. \qquad \textbf{Eq. 6-12}$$

$$\left.\left.-c_S^e)\,f_{c_L}^{L}(c_L)\right]\right)\frac{d\Upsilon}{dx}dx+\int_{-\lambda}^{\lambda}A^{S0}(\theta,c)\breve{q}'(\Upsilon)\frac{d\Upsilon}{dx}dx.$$

The first term of the right side of **Eq. 6-12**,

$$-\beta^{S0}\int_{-\lambda}^{\lambda}\frac{d^2\Upsilon}{dx^2}\frac{d\Upsilon}{dx}dx=\beta^{S0}\int_{0}^{0}\frac{d\Upsilon}{dx}d\left(\frac{d\Upsilon}{dx}\right)=0. \qquad \textbf{Eq. 6-13}$$

The middle term of the right side of **Eq. 6-12**,

$$\int_{-\lambda}^{\lambda}\left(q'(\Upsilon,a)\left[\Delta G_{S0}^{\theta}(\theta,c^e)-(c_L^e-c_S^e)f_{c_L}^{L}(c_L)\right]\right)\frac{d\Upsilon}{dx}dx$$

$$=\int_{1}^{0}\left[\Delta G_{S0}^{\theta}(\theta,c^e)-(c_L^e-c_S^e)f_c^S\left(c_S^i\right)\right]q'(\Upsilon,a)d\Upsilon$$

$$-\int_{1}^{0}(c_L^e-c_S^e)\left[V\int_{-\lambda}^{\lambda}\frac{\psi^l{}_{cc}}{D(\Upsilon)}\left[c(x)-c_S^i\right]dx\right]q'(\Upsilon,a)d\Upsilon. \qquad \textbf{Eq. 6-14}$$

$$\Rightarrow\int_{-\lambda}^{\lambda}\left(q'(\Upsilon,a)\left[\Delta G_{S0}^{\theta}(\theta,c^e)-(c_L^e-c_S^e)f_{c_L}^{L}(c_L)\right]\right)\frac{d\Upsilon}{dx}dx$$

$$=\Delta G_{S0}^{\theta}(\theta,c^e)-(c_L^e-c_S^e)f_c^S\left(c_S^i\right)$$

$$-\int_{1}^{0}(c_L^e-c_S^e)\left[V\int_{-\lambda}^{\lambda}\frac{\psi^l{}_{cc}}{D(\Upsilon)}\left[c(x)-c_S^i\right]dx\right]q'(\Upsilon,a)d\Upsilon,$$

The third term of the right side of **Eq. 6-12**,

$$\int_{-\lambda}^{\lambda} A^{S0}(\theta,c)\breve{q}'(\Upsilon)\frac{d\Upsilon}{dx}dx = A^{S0}(\theta,c)\int_{1}^{0}\breve{q}'(\Upsilon)d\Upsilon = 0. \qquad \textbf{Eq. 6-15}$$

Putting these values from **Eq. 6-13**, **Eq. 6-14** and **Eq. 6-15** in **Eq. 6-12**,

$$\frac{V}{L_\Upsilon}\int_{-\lambda}^{\lambda}\left(\frac{d\Upsilon}{dx}\right)^2 dx$$

$$= \Delta G_{S0}^{\theta}(\theta,c^e) - (c_L^e - c_S^e)f_c^S\left(c_S^i\right) \qquad \textbf{Eq. 6-16}$$

$$-\int_{1}^{0}(c_L^e - c_S^e)\left[V\int_{-\boldsymbol{\lambda}}^{\lambda}\frac{\psi^l{}_{cc}}{D(\Upsilon)}\left[c(x)-c_S^i\right]dx\right]q'(\Upsilon,a)d\Upsilon,$$

Now from **Eq. 3-14** for equilibrium condition,

$$\frac{dc}{d\Upsilon} = (c_S - c_L)q'(\Upsilon,a) \cong -(c_L^e - c_S^e)q'(\Upsilon,a). \qquad \textbf{Eq. 6-17}$$

So, **Eq. 6-16** can be rewritten as,

$$\frac{V}{L_\Upsilon}\int_{-\lambda}^{\lambda}\left(\frac{d\Upsilon}{dx}\right)^2 dx$$

$$= f^L(c_L^e) - f^S(c_S^e) - (c_L^e - c_S^e)f_c^S\left(c_S^i\right) \qquad \textbf{Eq. 6-18}$$

$$+\int_{c_S}^{c_L} V\left[\int_{-\boldsymbol{\lambda}}^{\lambda}\frac{\psi^l{}_{cc}}{D(\Upsilon)}\left[c(x)-c_S^i\right]dx\right]dc,$$

Now from **Eq. 6-16** we can show that,

$$\Delta G_{S0}^{\theta}(\theta,c^e) - (c_L^e - c_S^e)f_c^S\left(c_S^i\right) = \alpha V, \qquad \textbf{Eq. 6-19}$$

Where,

$$\alpha = \frac{1}{L_\Upsilon}\int_{-\lambda}^{\lambda}\left(\frac{d\Upsilon}{dx}\right)^2 dx \qquad \textbf{Eq. 6-20}$$

$$+\int_{1}^{0}(c_L^e - c_S^e)\left[\int_{-\boldsymbol{\lambda}}^{\lambda}\frac{\psi^l{}_{cc}}{D(\Upsilon)}\left[c(x)-c_S^i\right]dx\right]q'(\Upsilon,a)d\Upsilon.$$

Now from common tangent relation in equilibrium,

$$f_{c_L}^{L}(c_L^e) = f_{c_S}^{S}(c_S^e) = \frac{f^L(c_L^e) - f^S(c_S^e)}{c_L^e - c_S^e} = \frac{\Delta G_{S0}^{\theta}(\theta, c^e)}{c_L^e - c_S^e}. \qquad \textbf{Eq. 6-21}$$

Now from **Eq. 6-19**,

$$(c_L^e - c_S^e)\left[f_{c_S}^{S}(c_S^e) - f_c^S\left(c_S^i\right)\right] = \alpha V. \qquad \textbf{Eq. 6-22}$$

From dilute solution approximation,

$$f_{c_S}^{S}(c_S^e) - f_c^S\left(c_S^i\right) = \frac{RT}{v_m}\left(1 - \frac{c_S^i}{c_S^e}\right). \qquad \textbf{Eq. 6-23}$$

Now from **Eq. 6-22** and **Eq. 6-23**,

$$(c_L^e - c_S^e)\left[\frac{RT}{v_m}\left(1 - \frac{c_S^i}{c_S^e}\right)\right] = \alpha V$$

$$\Rightarrow (c_L^e - c_S^e)\left(1 - \frac{c_S^i}{c_S^e}\right) = V\frac{v_m}{RT}\alpha$$

$$\Rightarrow c_L^e - c_S^e - \frac{c_S^i}{c_S^e}.c_L^e + c_S^i = V\frac{v_m}{RT}\alpha$$

$$\Rightarrow c_L^e(1 - k^e) - \frac{c_S^i}{k^e}(1 - k^e) = V\frac{v_m}{RT}\alpha$$

$$\Rightarrow c_L^e m^e - m^e\frac{c_S^i}{k^e} = V\frac{v_m}{RT}\frac{\alpha m^e}{1 - k^e}$$

$$\Rightarrow T_m - T - m^e\frac{c_S^i}{k^e} = V\frac{v_m}{RT}\frac{\alpha m^e}{1 - k^e}$$

$$\Rightarrow T = T_m - m^e\frac{c_S^i}{k^e} - V\frac{v_m}{RT}\frac{\alpha m^e}{1 - k^e}$$

$$T = T_m - m^e\frac{c_S^i}{k^e} - V\beta, \qquad \textbf{Eq. 6-24}$$

Where $\beta = \frac{v_m}{RT}\frac{\alpha m^e}{1-k^e}$. **Eq. 6-24** is the relationship in classical sharp interface model between the temperature and composition.

CHAPTER 7

SOLUTE TRAPPING

Solute trapping is known as the dependence of jump in concentration through the interface on interface velocity. Across the moving interface, the chemical potential depends on the position. The equality of the chemical potential implies that there is no gradient along the interface. As the chemical potential varies across the moving interface solute trapping occurs. Here, a dilute solution is considered and diffusivity D_i is constant in both interfacial region and liquid, while it is neglected for the solid phase. For 1D instantaneous steady-state from **Eq. 6-2**, we have

$$-V\frac{\partial c}{\partial x} = \frac{d}{dx}\left[\frac{D_i}{\psi^l{}_{cc}}\frac{d}{dx}\frac{df^L(c_L)}{dc_L}\right]. \qquad \textbf{Eq. 7-1}$$

Here, V is the interface velocity. Integrating **Eq. 7-1**,

$$Vc(x) + \frac{D_i}{\psi^l{}_{cc}}\frac{d}{dx}\frac{df^L(c_L)}{dc_L} = A. \qquad \textbf{Eq. 7-2}$$

On the solid side interface, similarly from **Eq. 6-6**,

$$A = Vc_S^i. \qquad \textbf{Eq. 7-3}$$

Putting the value of A in **Eq. 7-2**,

$$\frac{d}{dx}\frac{df^L(c_L)}{dc_L} = -\frac{V}{D_i}\left(c - c_S^i\right)\psi^l{}_{cc}. \qquad \textbf{Eq. 7-4}$$

Now,

$$\frac{d}{dx}\frac{df^L(c_L)}{dc_L} = \frac{d^2f^L(c_L)}{dc_L{}^2}\frac{dc_L}{dx} = f_{cc}^L(c_L)\frac{dc_L}{dx}. \quad \textbf{Eq. 7-5}$$

Substituting the value from **Eq. 4-6**,

$$\frac{d}{dx}\frac{df^L(c_L)}{dc_L} = \frac{RT}{V_m}\frac{1}{(1-c_L)c_L}\frac{dc_L}{dx}. \quad \textbf{Eq. 7-6}$$

For dilute alloy, $(1-c_L) \to 1$ and $(1-c_S) \to 1$. So, from **Eq. 7-6**,

$$\frac{d}{dx}\frac{df^L(c_L)}{dc_L} = \frac{RT}{V_m}\frac{1}{c_L}\frac{dc_L}{dx}. \quad \textbf{Eq. 7-7}$$

And from **Eq. 4-16**,

$$\frac{c_S(x)}{c_L(x)} = \frac{c_S^e}{c_L^e} = k^e. \quad \textbf{Eq. 7-8}$$

Applying this relation in **Eq. 3-6**,

$$c(x) = [1-(1-k^e)q(\Upsilon,a)]c_L. \quad \textbf{Eq. 7-9}$$

Now from **Eq. 3-27**, **Eq. 4-6** and **Eq. 4-9**,

$$\psi^l{}_{cc} = \frac{RT}{v_m}\frac{\frac{1}{(1-c_L)c_L}\frac{1}{(1-c_S)c_S}}{[1-q(\Upsilon,a)]\frac{1}{(1-c_S)c_S} + q(\Upsilon,a)\frac{1}{(1-c_L)c_L}}. \quad \textbf{Eq. 7-10}$$

Simplifying,

$$\psi^l{}_{cc} = \frac{RT}{v_m[1-(1-k^e)q(\Upsilon,a)]c_L}. \quad \textbf{Eq. 7-11}$$

Putting the values from **Eq. 7-7** and **Eq. 7-11** in **Eq. 7-4**,

$$\frac{RT}{V_m}\frac{1}{c_L}\frac{dc_L}{dx} = -\frac{V}{D_i}\left(c - c_S^i\right)\frac{RT}{v_m[1-(1-k^e)q(\Upsilon,a)]c_L}. \quad \textbf{Eq. 7-12}$$

Putting the value of *c* from **Eq. 7-9** and simplifying **Eq. 7-12**,

$$\frac{dc_L}{dx} + \frac{V}{D_i}c_L = \frac{V}{D_i}\frac{c_S^i}{[1-(1-k^e)q(\Upsilon,a)]}. \quad \textbf{Eq. 7-13}$$

The **Eq. 7-13** can be rewritten as,

$$y'(x) + ay(x) = \frac{ab}{1-(1-c)f(x)}. \qquad \textbf{Eq. 7-14}$$

Where, $V/D_i = a$, $c_S^i = b$, $k^e = c$ and $q(\Upsilon, a) = f(x)$. The general solution of **Eq. 7-14**,

$$y(x) = ke^{-ax} + e^{-ax}\int_1^x \frac{abe^{ax'}}{1-(1-c)f(x')}\,dx'. \qquad \textbf{Eq. 7-15}$$

Putting the values of a, b and c in **Eq. 7-15**,

$$c_L(x) = ke^{-\frac{V}{D_i}x} + e^{-\frac{V}{D_i}x}\int_1^x \frac{\frac{V}{D_i}c_S^i e^{\frac{V}{D_i}x'}}{1-(1-k^e)q(x')}\,dx', \qquad \textbf{Eq. 7-16}$$

Under a boundary condition $c_L = \frac{c_S}{k^e} = c_S^i/k^e$ at $x = -\lambda$ we have

$$c_L(x) = \frac{c_S^i}{k^e}e^{-\frac{V}{D_i}(x+\lambda)} + \frac{V}{D_i}c_S^i e^{-\frac{V}{D_i}x}\int_{-\lambda}^x \frac{e^{\frac{V}{D_i}x'}}{1-(1-k^e)q(x')}\,dx'. \qquad \textbf{Eq. 7-17}$$

Putting the value in **Eq. 7-9**,

$$c(x) = [1-(1-k^e)q(\Upsilon,a)]\left[\frac{c_S^i}{k^e}e^{-\frac{V}{D_i}(x+\lambda)} + \frac{V}{D_i}c_S^i e^{-\frac{V}{D_i}x}\int_{-\lambda}^x \frac{e^{\frac{V}{D_i}x'}}{1-(1-k^e)q(x')}\,dx'\right]. \qquad \textbf{Eq. 7-18}$$

This equation expresses the partition coefficient as a function of interface velocity. Partition coefficient *k* is defined as the ratio of composition of the solid side of interface and composition at the liquid side of the interface or composition of the solid side of the interface to the maximum composition across the interface. **Eq. 7-18** can be rewritten in dimensionless form as,

$$\tilde{c}(x) = [1-(1-k^e)q(\Upsilon,a)]\left[\frac{1}{k^e}e^{-P\tilde{x}} + Pe^{-P\left(\tilde{x}+\frac{1}{2}\right)}\int_{-0.5}^{x}\frac{e^{P\tilde{x}'}}{1-(1-k^e)q(\Upsilon)}d\tilde{x}'\right], \quad \textbf{Eq. 7-19}$$

Where, $\tilde{x} = x/2\lambda$ and $\tilde{c} = c/c_S^i$. Here interface Péclet number $P = 2\lambda V/D$ controls partition coefficient *k*. Now[81],

$$\Upsilon(x) = \left[1 + e^{-\sqrt{\frac{A^{S0}(\theta,c)}{\beta^{S0}}}(x-x_o)}\right]^{-1}. \quad \textbf{Eq. 7-20}$$

We adopted α =2.94 and$k^e = 0.8$ with which ϕ changes from .05 to .95 at $-\lambda < x < \lambda$.

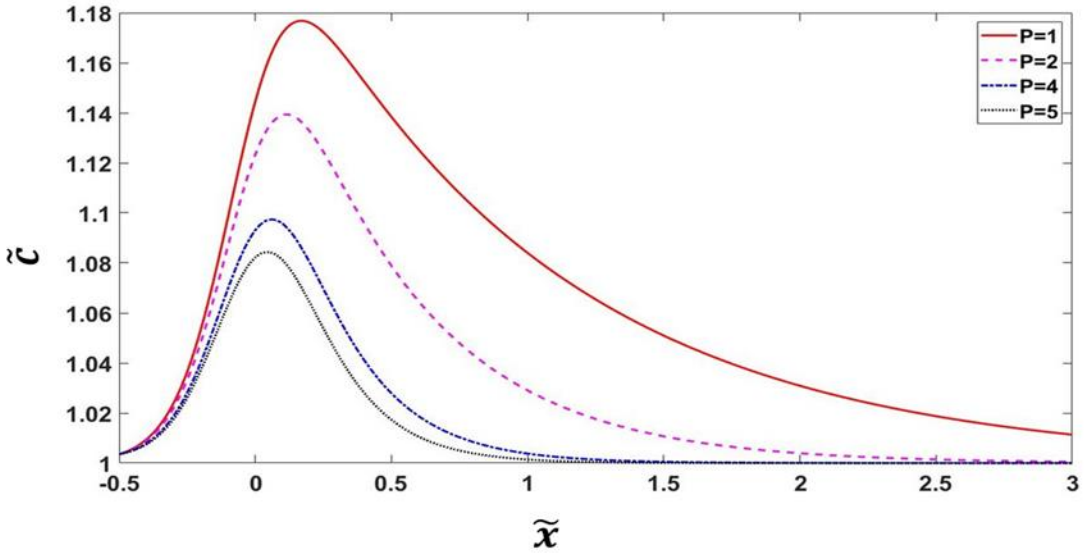

Figure 7-1: Variation of concentration profile for different values of P.

Figure 7-1 for a low value of *P*, the value of $\frac{c_{max}}{c_S^i}$ is close to equilibrium. With increasing *P*, the height of the concentration profile and thickness of the diffusive boundary layer decrease around the interface. **Figure 7-2** shows the variation of partition coefficient

as a function of *P*, which indicates the partition coefficient starts from 0.85 and gradually reaches 1 as *P* increases. From definition interface thickness can be defined as,

$$k(P) = \frac{k^e + \gamma P}{1 + \gamma P}. \qquad \textbf{Eq. 7-21}$$

where,

$$\gamma = \frac{8(1 - k^e)}{6\alpha l\, n\left(\frac{1}{k^e}\right)}. \qquad \textbf{Eq. 7-22}$$

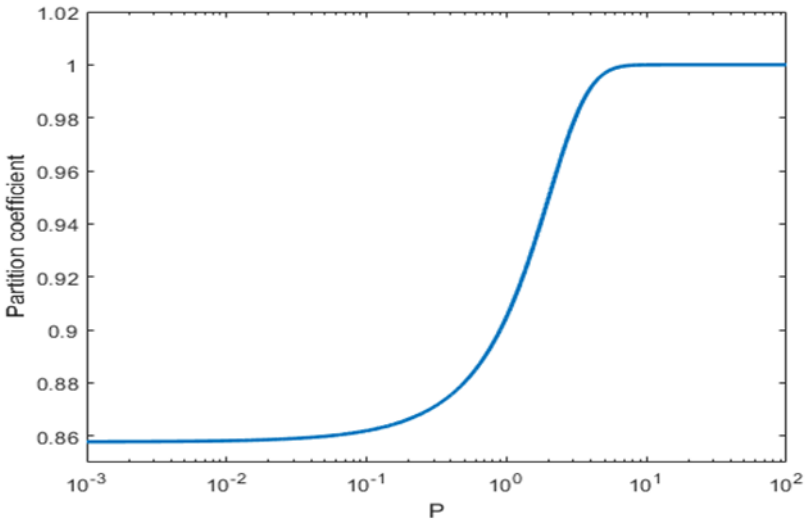

Figure 7-2: Variation of partition coefficient as a function of p.

Partitionless solidification occurs with complete solute trapping. Then interface temperature *T* is below T_o temperature when $f^S(c_S)$ and $f^L(c_L)$ becomes equal. For dilute solution condition can be written as,

$$T < T_o = T_m + c_\infty \frac{m^e ln k^e}{1 - k^e}. \qquad \textbf{Eq. 7-23}$$

Here, c_∞ is the bulk composition. During partitionless solidification, the interface velocity is expressed as, $(T_o - T)/\beta$ [82]. For dilute solution 1D phase field equation from **Eq. 4-13**, **Eq. 4-15** and **Eq. 6-1**,

$$-\frac{V}{L_\Upsilon}\frac{\partial \Upsilon}{\partial x} = -\left\{q'(\Upsilon,a)\frac{RT}{V_m}[(c_L^e - c_S^e) - (c_L - c_S)] + A^{S0}(\theta,c)\breve{q}'(\Upsilon)\right\} + \beta^{S0}\frac{d^2\Upsilon}{dx^2}. \quad \textbf{Eq. 7-24}$$

And for partitionless solidification, from **Eq. 7-9**,

$$c_L = \frac{c_\infty}{[1-(1-k^e)q(\Upsilon,a)]}, \quad \textbf{Eq. 7-25}$$

With approximation from **Eq. 7-8**,

$$-\frac{V}{L_\Upsilon}\frac{V_m}{RT}\frac{\partial \Upsilon}{\partial x} = -\left\{q'(\Upsilon,a)c_L^e(1-k^e) - q'(\Upsilon,a)\frac{c_\infty(1-k^e)}{[1-(1-k^e)q(\Upsilon,a)]} + A^{S0}(\theta,c)\breve{q}'(\Upsilon)\right\} + \beta^{S0}\frac{d^2\Upsilon}{dx^2}, \quad \textbf{Eq. 7-26}$$

Now,

$$\frac{d}{d\Upsilon}ln[1-(1-k^e)q(\Upsilon,a)] = -q'(\Upsilon,a)\frac{(1-k^e)}{[1-(1-k^e)q(\Upsilon,a)]}, \quad \textbf{Eq. 7-27}$$

Putting the value in **Eq. 7-26**,

$$-\frac{V}{L_\Upsilon}\frac{V_m}{RT}\frac{\partial \Upsilon}{\partial x} = -\left\{q'(\Upsilon,a)c_L^e(1-k^e) + c_\infty\frac{d}{d\Upsilon}ln[1-(1-k^e)q(\Upsilon,a)] + A^{S0}(\theta,c)\breve{q}'(\Upsilon)\right\} + \beta^{S0}\frac{d^2\Upsilon}{dx^2}, \quad \textbf{Eq. 7-28}$$

Multiplying with $\frac{\partial \Upsilon}{\partial x}$ on both sides and integrate from $x = -\infty$ to $x = +\infty$,

$$-\frac{V}{L_\Upsilon}\frac{V_m}{RT}\int_{-\infty}^{+\infty}\left(\frac{\partial \Upsilon}{\partial x}\right)^2 dx$$

$$= -\int_{-\infty}^{+\infty} q'(\Upsilon,a)c_L^e(1-k^e)\frac{\partial \Upsilon}{\partial x}dx$$

$$-\int_{-\infty}^{+\infty} c_\infty \frac{d}{d\Upsilon} ln[1-(1-k^e)q(\Upsilon,a)]\frac{\partial \Upsilon}{\partial x}dx \qquad \textbf{Eq. 7-29}$$

$$-\int_{-\infty}^{+\infty} A^{S0}(\theta,c)\breve{q}'(\Upsilon)\frac{\partial \Upsilon}{\partial x}dx + \int_{-\infty}^{+\infty}\beta^{S0}\frac{d^2\Upsilon}{dx^2}\frac{\partial \Upsilon}{\partial x}dx,$$

Similarly, from **Eq. 6-13** and **Eq. 6-15**,

$$\int_{-\infty}^{+\infty} A^{S0}(\theta,c)\breve{q}'(\Upsilon)\frac{\partial \Upsilon}{\partial x}dx = 0, \qquad \textbf{Eq. 7-30}$$

and,

$$\int_{-\infty}^{+\infty}\beta^{S0}\frac{d^2\Upsilon}{dx^2}\frac{\partial \Upsilon}{\partial x}dx = 0. \qquad \textbf{Eq. 7-31}$$

Now,

$$\int_{-\infty}^{+\infty} q'(\Upsilon,a)c_L^e(1-k^e)\frac{\partial \Upsilon}{\partial x}dx = \int_0^1 q'(\Upsilon,a)c_L^e(1-k^e)d\Upsilon. \qquad \textbf{Eq. 7-32}$$

And,

$$\int_{-\infty}^{+\infty} c_\infty \frac{d}{d\Upsilon} ln[1-(1-k^e)q(\Upsilon,a)]\frac{\partial \Upsilon}{\partial x}dx$$

$$= \int_0^1 c_\infty \frac{d}{d\Upsilon} ln[1-(1-k^e)q(\Upsilon,a)]d\Upsilon = c_\infty lnk^e, \qquad \textbf{Eq. 7-33}$$

Putting the values,

$$\frac{V}{L_\Upsilon}\frac{V_m}{RT}\int_{-\infty}^{+\infty}\left(\frac{\partial \Upsilon}{\partial x}\right)^2 dx = c_L^e(1-k^e) + c_\infty lnk^e, \qquad \textbf{Eq. 7-34}$$

Therefore, the condition for partitionless solidification is,

$$c_L^e(1-k^e) + c_\infty lnk^e > 0. \qquad \textbf{Eq. 7-35}$$

CHAPTER 8

THERMODYNAMIC EQUILIBRIUM AND STABILITY CONDITION FOR HOMOGENOUS STATE

From **Eq. 3-19** we get,

$$\psi^{l}{}_{\Upsilon} = q'(\Upsilon, a)\left[\Delta G^{\theta}_{S0}(\theta, c) + \frac{\partial f^{L}(c_L)}{\partial c_L}(c_S^B - c_L^B)\right] + A^{S0}(\theta, c)\breve{q}'(\Upsilon) + \breve{q}(\Upsilon)\frac{\partial A^{S0}(\theta, c)}{\partial c}(c_S^B - c_L^B)q'(\Upsilon, a), \quad \textbf{Eq. 8-1}$$

For simplicity let us assume $A^{S0}(\theta, c)$ is constant. So $\frac{\partial A^{S0}(\theta,c)}{\partial c} = 0$.

$$\psi^{l}{}_{\Upsilon} = q'(\Upsilon, a)\left[\Delta G^{\theta}_{S0}(\theta, c) + \frac{\partial f^{L}(c_L)}{\partial c_L}(c_S^B - c_L^B)\right] + A^{S0}(\theta, c)\breve{q}'(\Upsilon), \quad \textbf{Eq. 8-2}$$

Differentiating **Eq. 8-2** with respect to Υ we have,

$$\psi^{l}{}_{\Upsilon\Upsilon} = q''(\Upsilon, a)\left[\Delta G^{\theta}_{S0}(\theta, c) + \frac{\partial f^{L}(c_L)}{\partial c_L}(c_S^B - c_L^B)\right] + q'(\Upsilon, a)\frac{\partial}{\partial \Upsilon}\left[\Delta G^{\theta}_{S0}(\theta, c) + \frac{\partial f^{L}(c_L)}{\partial c_L}(c_S^B - c_L^B)\right] + A^{S0}(\theta, c)\breve{q}''(\Upsilon), \quad \textbf{Eq. 8-3}$$

Assuming $a = 0$, we have,

$$q(\Upsilon) = 4\Upsilon^3 - 3\Upsilon^4,$$
$$q'(\Upsilon) = 12\Upsilon^2 - 12\Upsilon^3, \quad \textbf{Eq. 8-4}$$
$$q''(\Upsilon) = 24\Upsilon - 36\Upsilon^2.$$

We calculate the values at $\Upsilon = 0$ and $\Upsilon = 1$,

$$q(\Upsilon = 0) = 0; \quad q'(\Upsilon = 0) = 0; \quad q''(\Upsilon = 0) = 0,$$
$$q(\Upsilon = 1) = 1; \quad q'(\Upsilon = 1) = 0; \quad q''(\Upsilon = 1) = -12. \qquad \textbf{Eq. 8-5}$$

Again we have,

$$\breve{q}(\Upsilon) = \Upsilon^2(1-\Upsilon)^2,$$
$$\breve{q}'(\Upsilon) = 2\Upsilon - 6\Upsilon^2 + 4\Upsilon^3, \qquad \textbf{Eq. 8-6}$$
$$\breve{q}''(\Upsilon) = 2 - 12\Upsilon + 12\Upsilon^2.$$

We calculate the values at $\Upsilon = 0$ and $\Upsilon = 1$,

$$\breve{q}(\Upsilon = 0) = 0; \quad \breve{q}'(\Upsilon = 0) = 0; \quad \breve{q}''(\Upsilon = 0) = 2,$$
$$\breve{q}(\Upsilon = 1) = 0; \quad \breve{q}'(\Upsilon = 0) = 0; \quad \breve{q}''(\Upsilon = 0) = 2. \qquad \textbf{Eq. 8-7}$$

So From **Eq. 8-3**,

$$\frac{\partial^2 \psi^l}{\partial \Upsilon^2} = A^{S0}(\theta, c), \qquad \textbf{Eq. 8-8}$$

$$\frac{\partial^2 \psi^l}{\partial \Upsilon^2} = A^{S0}(\theta, c) - 6\left[\Delta G^{\theta}_{S0}(\theta, c) + \frac{\partial f^L(c_L)}{\partial c_L}(c_S^B - c_L^B)\right], \qquad \textbf{Eq. 8-9}$$

Eq. 8-8 and **Eq. 8-9** gives the value of $\frac{\partial^2 \psi^l}{\partial \Upsilon^2}$ at $\Upsilon = 0$ and $\Upsilon = 1$ respectively.

Now at, $\Upsilon = 0$ $M \rightarrow S$ phase transformation,

$$\frac{\partial^2 \psi^l}{\partial \Upsilon^2} \leq 0,$$
$$A^{S0} \leq 0. \qquad \textbf{Eq. 8-10}$$

Now at $\Upsilon = 1$ $S \rightarrow M$ phase transformation,

$$\frac{\partial^2 \psi^l}{\partial \Upsilon^2} \leq 0,$$
$$A^{S0} - 6\left[\Delta G^{\theta}_{S0}(\theta, c) + \frac{\partial f^L(c_L)}{\partial c_L}(c_S^B - c_L^B)\right] \leq 0, \qquad \textbf{Eq. 8-11}$$

Now let $\Delta G_{S0}^{\theta}(\theta, c) = -\Delta S_{S0}(\theta - \theta_e^{S0})$, here $\Delta S_{S0} < 0$ is the difference in entropy between the solid and liquid phases. θ_e^{S0} is the thermodynamic equilibrium melting temperature of the solid. The loss of stability of melt to solid is, $A^{S0} = A_c^{S0}(\theta - \theta_c^{S0})$. θ_c^{S0} is the critical temperature where liquid loses it's stability.

CHAPTER 9

NUMERICAL SIMULATION

Let us consider a 1D isothermal system with uniform bulk modulus. The system temperature with undercooling is given. When the system temperature is lower than the solidus, the system can reach a steady state. The system can also reach a steady state when a solute sink exists and sweep over all solute influx from its neighbors. The classical sharp interface model with negligible diffusivity in solid can be described by [83],

$$-V\frac{dc}{dx} = D_L\frac{d^2c}{dx^2}, \qquad \textbf{Eq. 9-1}$$

$$V(1-k^e)c^i = -D_L\frac{dc}{dx}, \qquad \textbf{Eq. 9-2}$$

$$T = T_m - m^e c^i - \beta V, \qquad \textbf{Eq. 9-3}$$

$$c(\xi^*) = c_\infty. \qquad \textbf{Eq. 9-4}$$

Here, ξ^* is denoted as the distance between the solute sink and the interface. c^i is the concentration at the interface. The exact solution of **Eq. 9-1**, **Eq. 9-2**, **Eq. 9-3** and **Eq. 9-4** is,

$$c(x) = c_\infty + c_\infty\frac{(1-k^e)(e^{-\frac{Vx}{D_L}} - e^{-\frac{V\xi^*}{D_L}})}{1-(1-k^e)(1-e^{-\frac{V\xi^*}{D_L}})}, \qquad \textbf{Eq. 9-5}$$

Then the interface velocity is determined by,

$$\beta V = T_m - T - \frac{m^e c_\infty}{1-(1-k^e)\left(1-e^{-\frac{V\xi^*}{D_L}}\right)}, \qquad \textbf{Eq. 9-6}$$

In **Eq. 9-6** $\xi^* \to \infty$ implies that interface velocity is positive if solidus temperature T_{Sol} is greater that temperature T, here $T_{Sol} = T_m - m^e c_\infty / k^e$. And when ξ^* has finite value, the interface velocity is positive if the liquidus temperature is greater than the temperature T, here $T_{Liq} = T_m - m^e c_\infty$. Again, exact solution for partitionless solidification is available. In this case, the interface velocity is given by,

$$V = \frac{T_0 - T}{\beta}, \qquad \textbf{Eq. 9-7}$$

T_0 is the temperature where free energies of solid and liquid becomes equal. For computational work, we considered a diluted solution. **Eq. 3-9**, **Eq. 3-25** and **Eq. 3-31** are used for our model with $q(\Upsilon) = 4\Upsilon^3 - 3\Upsilon^4$. The model system was chosen to be Ni-Cu (0.05 mole fraction alloy). The material parameters used for computation are as follows: $D_S = 1 * 10^{-14} m^2/s,\ D_L = 1 * 10^{-9} m^2/s,\ T_m = 1728.0K, k^e = 0.7965,\ m^e = 310.9,$ $T_{Sol} = 1708.5K, T_{Liq} = 1712.5K,\ \sigma = 0.37 J/m^2,\ \beta = 10 Ks/m$, the grid size was 1nm and between the interface the phase field vary from 0.05 to 0.95. From **Eq. 9-6**, **Eq. 9-3**, **Eq. 6-24** and **Eq. 9-7** putting the value of T_{Sol} and **Eq. 7-23**, the relations of interface velocity is expressed as,

$$\beta V = T_{Sol} - T, \qquad \textbf{Eq. 9-8}$$

$$\beta V = T_{Sol} - T + m^e \left(\frac{c_\infty}{k^e} - c^i\right), \qquad \textbf{Eq. 9-9}$$

$$\beta V = T_{Sol} - T + m^e c_\infty \left(\frac{1}{k^e} + \frac{ln k^e}{1-k^e}\right), \qquad \textbf{Eq. 9-10}$$

$$\beta V = T_{Sol} - T + \frac{m^e}{k^e}\left(c_\infty - c_S^i\right), \qquad \textbf{Eq. 9-11}$$

Here **Eq. 9-8** is for analytical solution for classical sharp interface mode. **Eq. 9-9** is the sharp interface model with diffusion in liquid only. **Eq. 9-10** is the analytical solution for partitionless solidification. **Eq. 9-11** is for thin interface limit at low Péclet number condition.

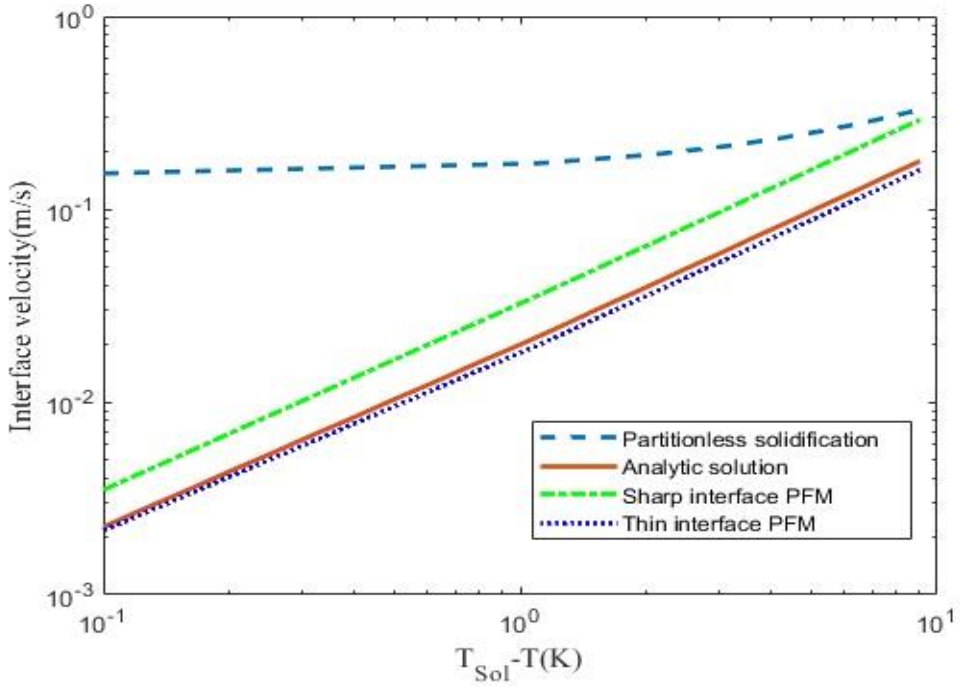

Figure 9-1: Variation of interface velocity, calculated at $\xi^* \to \infty$ as a function of $T_{Sol} - T$

Figure 9-1 shows the variation of interface velocity as a function of undercooling $T_{Sol} - T$ ignoring the solute sink ($\xi^* \to \infty$). The solid straight line shows the analytical solution of **Eq. 9-6**. The curved dashed line shows the analytical solution of partitionless solidification $V = (T_0 - T)/\beta$. The dotted line and the green line are calculated from the thin interface limit and sharp interface limit. For a thin interface, limit the interface velocity

marge with an analytical solution as undercooling decreases. At large undercooling, the interface velocity of sharp interface limit is close to the analytical solution of partitionless solidification.

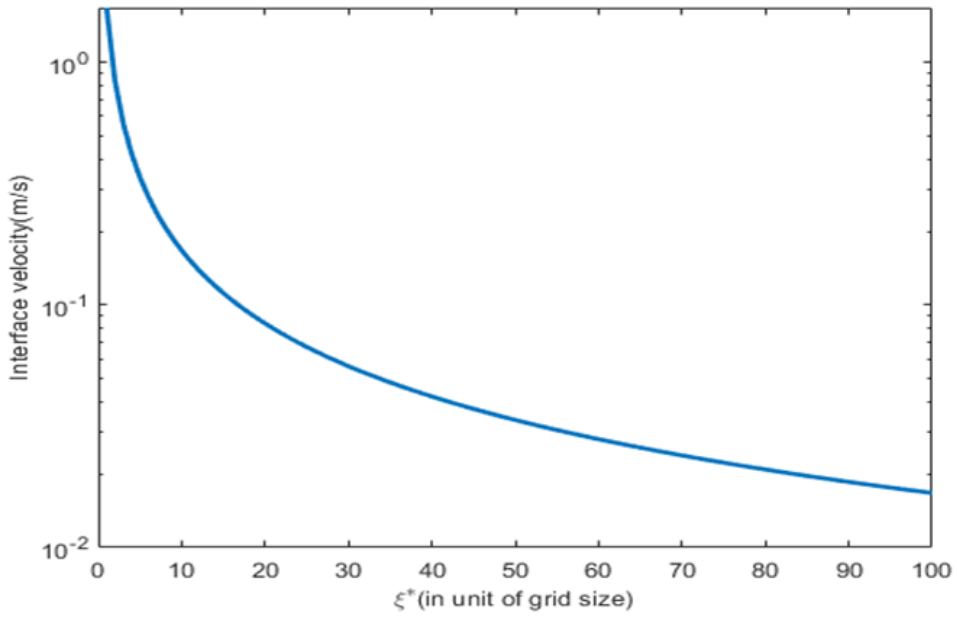

Figure 9-2: Variation of interface velocity calculated neglecting kinetic effect as a function of ξ^*.

In **Figure 9-2** we can observe the variation of interface velocity as a function of the distance between interface and solute sink ξ^*. Here we neglect the kinetic coefficient. The system temperature was 1709K. The curved line shows the analytical solution of **Eq. 9-6**. The physical meaning of zero kinetic coefficients in thin interface alloy PFM means a decrease of solid composition by phase field alloy or increase of the solid composition by interface thickness, bringing the solute trapping effect increases the solid composition.

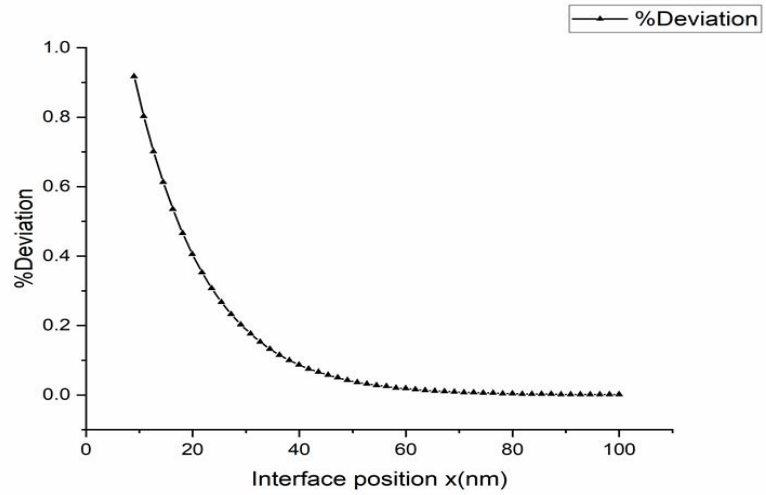

Figure 9-3: Variation of solid composition along with the interface.

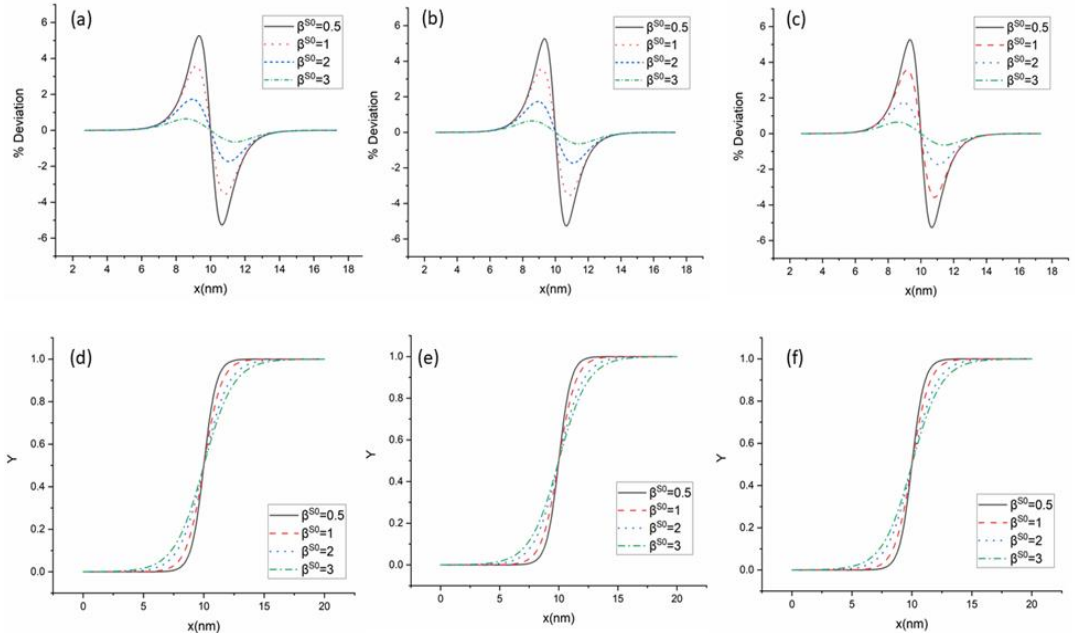

Figure 9-4: Deviation of solid composition along with the interface with dimentionless diffusivity $(a)\ D* = 1,\ (b)\ D* = 2\ (c)\ D* = 5$ and variation of Υ along with the interface with dimentionless diffusivity $(a)\ D* = 1,\ (b)\ D* = 2\ (c)\ D* = 5$

Figure 9-3 shows the variation in solid composition along with the interface for $\Upsilon < 0.5$. The vertical axis represents the relative difference between the measured solid

composition at the interface c_S^i and the equilibrium composition c_S^e, scaled by the equilibrium composition c_S^e. **Figure 9-4** (a), (b) and (c) show the change in variation of solid composition with a coefficient of phase field gradient energy, β^{S0} along the interface for : $D* = 1,\ D* = 2\ and\ D* = 5$ respectively. Here $D*$ is the dimentionless diffusivity As the coefficient of gradient energy increases, the height of the variation decreases. So, with high gradient energy the solid interface composition c_S^i approaches to equilibrium solid concentration c_S^e. Again, **Figure 9-4** (d), (e) and (d) shows the change in Υ with a coefficient of phase field gradient energy along with the interface for : $D* = 1,\ D* = 2\ and\ D* = 5$ respectively. From the plot, we can see that as the coefficient of gradient energy decreases, the phase field model tense to a sharp interface. **Figure 9-5** a and b shows the deviation of solid composition at the interface with diffusivity: $D* = 1,\ D* = 2\ and\ D* = 5$ for $\beta^{S0} = 1$ and $\beta^{S0} = 2$ respectively. From the figure, we can say that diffusivity has no effect on solid composition in the interface region.

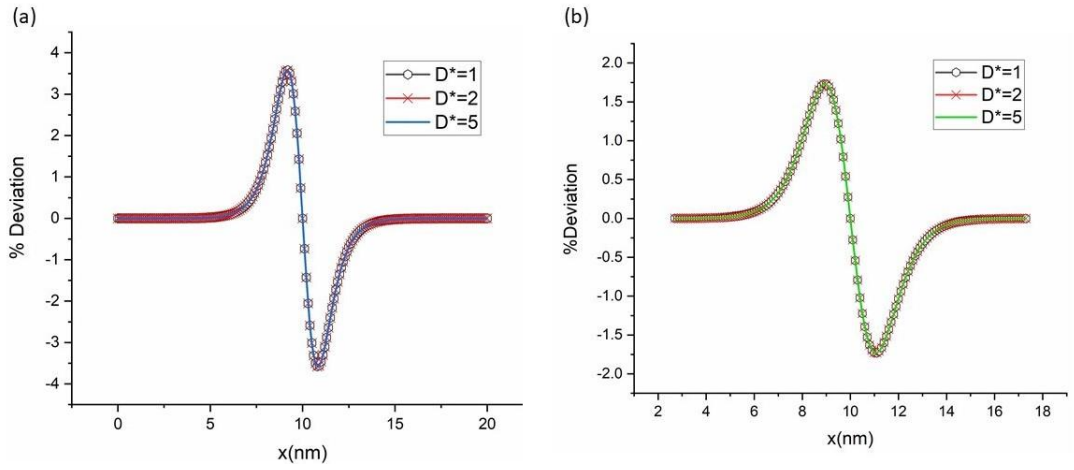

Figure 9-5: Deviation of solid composition along the interface with dimentionless diffusivity $D* = 1,\ D* = 2\ and\ D* = 5$ for (a) $\beta^{S0} = 1$ (b) $\beta^{S0} = 2$.

Now, for the validation of our simulation with the analytical result we use the analytical solution of GL equation **Eq. 5-20** and simulation result of Y with same material properties. **Figure 9-6** shows that the analytical solution coincides with the simulation result. So the simulation results were very good compare to analytical results.

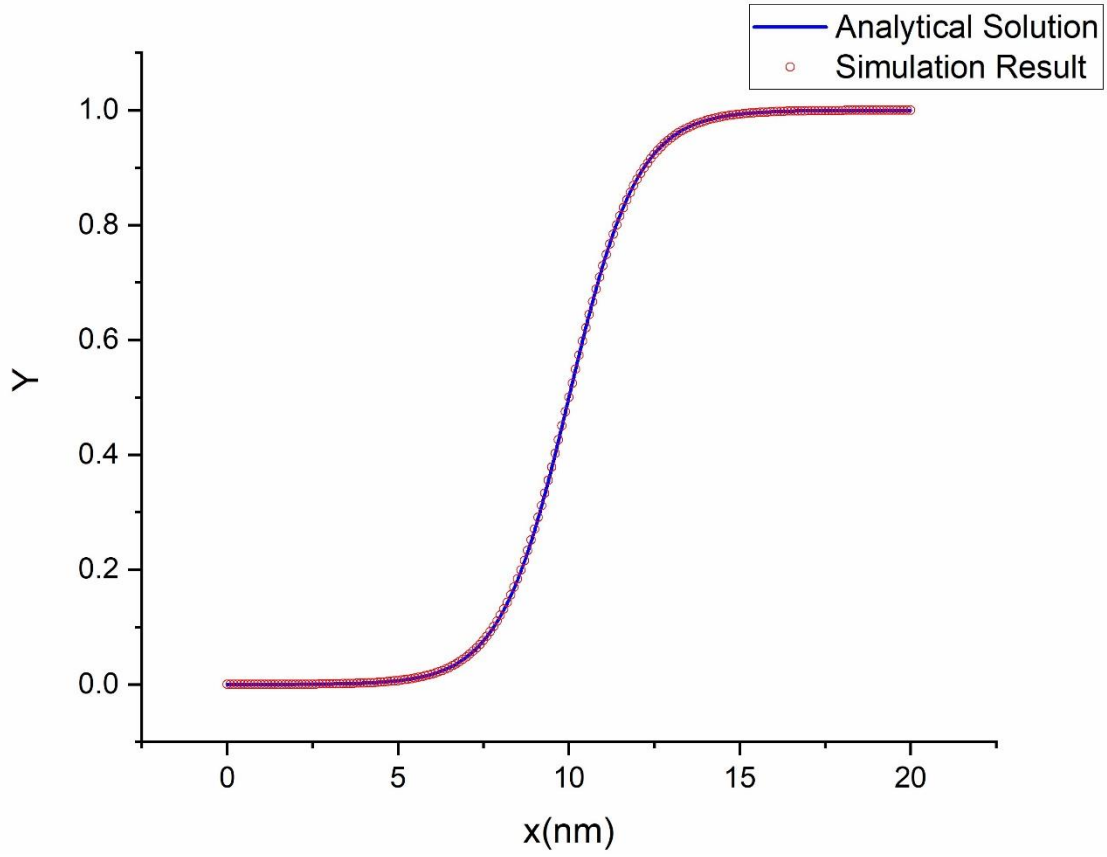

Figure 9-6: Comparison of numerical result with analytical result.

CHAPTER 10

CONCLUSIONS AND FUTURE WORK

We developed a PFM to demonstrate the phenomena of solidification in a binary alloy. The total energy of this model is the combination of free energy and gradient energy. Ginzburg-Landau equation and Cahn-Hilliard equation are adapted for free energy and gradient energy, where free energy is a combination of thermal energy and energy barrier. The PFM was reformulated for the dilute approximation limit. Then the solution of the Ginzburg-Landau equation was derived.

For the thin-interface limit, with the assumption of negligible diffusivity in the solid, the relationship between the kinetic coefficient and mobility was developed. From observation we can see that the solid composition tends to increase with the effect of finite interface thickness and decrease with finite phase field mobility. With zero kinetic coefficient, both these effects are canceled out that results in equilibrium at the interface.

Using this model for 1D steady state dilute solution with negligible diffusivity, we observed the concentration profile as a function of Péclet number which is a function of interface velocity. From the analytical solution it is concluded that with increasing interface velocity the concentration profile decreases. The distribution of partition coefficient was also obtained. From the relation between interface velocity and partition coefficient we can see that with high interface velocity the value of partition coefficient goes close to unity for sharp interface PFM. For 1D dilute solution we performed numerical simulations. From

simulation results we can conclude that the height of concentration profile is inversely propotional to coefficient of gradient energy.

For future work, we can develop a phase-field model that takes place between three-phase considering the simple thermodynamic potential for different conditions like thin interface model, sharp interface model, and solute trapping condition. We can also consider the effect of stress on phase transformation. Further, along with the numerical simulations, the experimental procedure can be carried out to validate the mathematical model.

APPENDIX A

MATLAB AND MOOSE CODES

A.1 Common Tangent Plot

```
syms l s x

fl(l) = (7233.18*(l.*log(l)+(1-l).*(log(1-l)))+l.*(-12281.41-6922.78*(1-l*2)+270*(1-l*6+(l*2)*6)).*(1-l))/0.0000106;

dfl(l) = diff(fl,l);
fs(s) = (-734.8*(1-s)+10544.4*s+7233.18*(s.*log(s)+(1-s).*(log(1-s)))-6806.78*s.*(1-s))/0.0000106;
dfs(s) = diff(fs,s);
eqns = [dfl(l)- dfs(s) == 0, (s - l)*dfl(l) == fs(s)-fl(l)];
[Sol_s, Sol_l] = vpasolve(eqns,[s l],[0.005 0.08]);
m=dfl(Sol_l);
c=fl(Sol_l)-m*Sol_l;
f1 = (-734.8*(1-x)+10544.4*x+7233.18*(x.*log(x)+(1-x).*(log(1-x)))-6806.78*x.*(1-x))/0.0000106;
f2=(7233.18*(x.*log(x)+(1-x).*(log(1-x)))+x.*(-12281.41-6922.78*(1-x*2)+270*(1-x*6+(x*2)*6)).*(1-x))/0.0000106;
```

```
y=m*x+c;

fplot (f1,[0.001 0.99]);

hold on

fplot (f2,[0.001 0.99]);

hold on

fplot (y,[0.001 0.99]);

ylabel('free energy density')

xlabel('concentration')

hold off
```

A.2 Moose Code

```
[Mesh]

  type = GeneratedMesh

  dim = 2

  elem_type = QUAD4

  nx = 10000

  ny = 2

  nz = 0

  xmin = 0

  xmax = 100

  ymin = 0

  ymax = 0.4

  zmin = 0
```

```
  zmax = 0
[]

[AuxVariables]
  [Fglobal]
    order = CONSTANT
    family = MONOMIAL
  []
[]

[Variables]
    [eta]
    order = FIRST
    family = LAGRANGE
  []
  [c]
    order = FIRST
    family = LAGRANGE
  []
  [w]
    order = FIRST
    family = LAGRANGE
  []
```

```
  [cl]
    order = FIRST
    family = LAGRANGE
    initial_condition = 0.05
  []
  [cs]
    order = FIRST
    family = LAGRANGE
    initial_condition = 0.95
  []
[]

[Functions]
  [ic_func_eta]
    type = ParsedFunction
    value = '(0.5*(2.0-tanh((x-10)/sqrt(2.0))+tanh((x-90)/sqrt(2.0))))'
  []
  [ic_func_c]
    type = ParsedFunction
    value = '.68*(0.5*(2.0-tanh((x-10)/sqrt(2.0))+tanh((x-90)/sqrt(2.0))))+0.85*(1-
(0.5*(2.0-tanh((x-10)/sqrt(2.0))+tanh((x-90)/sqrt(2.0)))))'
  []
[]
```

```
[ICs]
  [eta]
    type = FunctionIC
    variable = eta
    function = ic_func_eta
  []
  [c]
    type = FunctionIC
    variable = c
    function = ic_func_c
  []
[]

[BCs]
  inactive = 'left_c left_eta'
  [left_c]
    type = DirichletBC
    variable = c
    boundary = 'left'
    value = 0.5
  []
  [left_eta]
```

```
    type = DirichletBC
    variable = eta
    boundary = 'left'
    value = 0.5
  []
  [Periodic]
    [eta_c]
      variable = 'eta c w cl cs'
      auto_direction = 'x y'
    []
  []
[]

[Materials]
    [fl]
    type = DerivativeParsedMaterial
    f_name = fl
    args = 'cl'
    function = (0.85-cl)^2
  []
  [fs]
    type = DerivativeParsedMaterial
    f_name = fs
```

```
  args = 'cs'
  function = (0.68-cs)^2
[]
[h_eta]
  type = SwitchingFunctionMaterial
  h_order = HIGH
  eta = 'eta'
[]
[g_eta]
  type = BarrierFunctionMaterial
  g_order = SIMPLE
  eta = 'eta'
[]
[constants]
  type = GenericConstantMaterial
  prop_names = 'L   eps_sq'
  prop_values = '0.5 1'
[]
[D_eta]
  type = DerivativeParsedMaterial
  function = p
  f_name = p
  args = 'eta'
```

```
  material_property_names = 'p:=(0.00000000000001*h+0.000000001*(1-h))'
[]
[flcl]
  type = DerivativeParsedMaterial
  function = d2FL
  f_name = FL
  args = 'cl'
  material_property_names = 'd2FL:=D[fl(cl),cl,cl]'
[]
[fscs]
  type = DerivativeParsedMaterial
  function = d2FS
  f_name = FS
  args = 'cs'
  material_property_names = 'd2FS:=D[fs(cs),cs,cs]'
[]
[Mobility]
  type = DerivativeParsedMaterial
  function = d2F
  f_name = M
  args = 'eta c cl cs w'
  material_property_names = 'd2F:=(FS*h+FL*(1-h))*1*D/(FS*FL)'
[]
```

```
[]

[Kernels]
  [PhaseConc]
  type = KKSPhaseConcentration
  ca = 'cl'
  variable = cs
  c = 'c'
  eta = 'eta'
 []
 [ChemPotSolute]
  type = KKSPhaseChemicalPotential
  variable = cl
  cb = 'cs'
  fa_name = fl
  fb_name = fs
 []
 [CHBulk]
  type = KKSSplitCHCRes
  variable = c
  ca = 'cl'
  cb = 'cs'
  fa_name = fl
```

```
  fb_name = fs
  w = 'w'
[]
[dcdt]
  type = CoupledTimeDerivative
  variable = w
  v = 'c'
[]
[ckernel]
  type = SplitCHWRes
  mob_name = M
  variable = w
[]
[ACBulkF]
  type = KKSACBulkF
  variable = eta
  fa_name = fl
  fb_name = fs
  w = 1.0
  args = 'cl cs'
[]
[ACBulkC]
  type = KKSACBulkC
```

```
    variable = eta
    ca = 'cl'
    cb = 'cs'
    fa_name = fl
    fb_name = fs
  []
  [ACInterface]
    type = ACInterface
    variable = eta
    kappa_name = eps_sq
  []
  [detadt]
    type = TimeDerivative
    variable = eta
  []
[]

[AuxKernels]
  [GlobalFreeEnergy]
    type = KKSGlobalFreeEnergy
    variable = Fglobal
    fa_name = fl
    fb_name = fs
```

```
    w = 1.0
  []
[]

[Executioner]
  type = Transient
  solve_type = PJFNK
  petsc_options_iname = '-pc_type -sub_pc_type -sub_pc_factor_shift_type'
  petsc_options_value = 'asm      ilu          nonzero'
  l_max_its = 100
  nl_max_its = 100
  nl_abs_tol = 1e-10
  end_time = 800
  dt = 4.0
[]

[Preconditioning]
  [full]
    type = SMP
    full = true
  []
[]
```

```
[Postprocessors]
  [dofs]
    type = NumDOFs
  []
  [integral]
    type = ElementL2Error
    variable = 'eta'
    function = ic_func_eta
  []
[]

[Outputs]
  exodus = true
  console = true
  gnuplot = true
[]
```

BIBLIOGRAPHY

[1] A. C. F. on A. M. Technologies and A. C. F. on A. M. T. S. F. 91 on Terminology, *Standard terminology for additive manufacturing technologies*. ASTM International, 2012.

[2] C. K. Chua, C. H. Wong, and W. Y. Yeong, *Standards, quality control, and measurement sciences in 3D printing and additive manufacturing*. Academic Press, 2017.

[3] M. O. John, "Photo-glyph recording." Google Patents, Dec. 25, 1956.

[4] P. A. Ciraud, "Process and Device for the Manufacture of any Objects Desired from any Meltable Material," *FRG Discl. Publ.*, vol. 2263777, 1972.

[5] T. Nakagawa, "Blanking tool by stacked bainite steel plates," *Press Tech.*, pp. 93–101, 1979.

[6] M. Shellabear and O. Nyrhilä, "DMLS-Development history and state of the art," *Laser Assist. Netshape Eng. 4, Proc. 4th LANE*, pp. 21–24, 2004.

[7] N. S. and T. C. (US), *Materials genome initiative for global competitiveness*. Executive Office of the President, National Science and Technology Council, 2011.

[8] J. D. van der Waals, "The thermodynamic theory of capillarity under the hypothesis of a continuous variation of density," *J. Stat. Phys.*, vol. 20, no. 2, pp. 200–244, 1979.

[9] M. Lecture, "Spinodal Decomposition," vol. 242, no. February, 1968.

[10] J. W. Cahn and J. E. Hilliard, "Free energy of a nonuniform system. I. Interfacial free energy," *J. Chem. Phys.*, vol. 28, no. 2, pp. 258–267, 1958.

[11] J. W. Cahn and S. M. Allen, "A microscopic theory for domain wall motion and its experimental verification in Fe-Al alloy domain growth kinetics," *Le J. Phys. Colloq.*, vol. 38, no. C7, pp. C7-51, 1977.

[12] A. A. Wheeler, W. J. Boettinger, and G. B. McFadden, "Phase-field model for isothermal phase transitions in binary alloys," *Phys. Rev. A*, vol. 45, no. 10, p.

7424, 1992.

[13] A. A. Wheeler, W. J. Boettinger, and G. B. McFadden, “Phase-field model of solute trapping during solidification,” *Phys. Rev. E*, vol. 47, no. 3, p. 1893, 1993.

[14] J. Tiaden, B. Nestler, H.-J. Diepers, and I. Steinbach, “The multiphase-field model with an integrated concept for modelling solute diffusion,” *Phys. D Nonlinear Phenom.*, vol. 115, no. 1–2, pp. 73–86, 1998.

[15] K. Glasner, “Solute trapping and the non-equilibrium phase diagram for solidification of binary alloys,” *Phys. D Nonlinear Phenom.*, vol. 151, no. 2–4, pp. 253–270, 2001.

[16] Z. Bi and R. F. Sekerka, “Phase-field model of solidification of a binary alloy,” *Phys. A Stat. Mech. its Appl.*, vol. 261, no. 1–2, pp. 95–106, 1998.

[17] I. Loginova, G. Amberg, and J. Ågren, “Phase-field simulations of non-isothermal binary alloy solidification,” *Acta Mater.*, vol. 49, no. 4, pp. 573–581, 2001.

[18] J. C. Ramirez and C. Beckermann, “Examination of binary alloy free dendritic growth theories with a phase-field model,” *Acta Mater.*, vol. 53, no. 6, pp. 1721–1736, 2005.

[19] J. C. Ramirez, C. Beckermann, A. Karma, and H.-J. Diepers, “Phase-field modeling of binary alloy solidification with coupled heat and solute diffusion,” *Phys. Rev. E*, vol. 69, no. 5, p. 51607, 2004.

[20] M. Greenwood, N. Provatas, and J. Rottler, “Free energy functionals for efficient phase field crystal modeling of structural phase transformations,” *Phys. Rev. Lett.*, vol. 105, no. 4, pp. 1–4, 2010, doi: 10.1103/PhysRevLett.105.045702.

[21] M. Greenwood, N. Ofori-Opoku, J. Rottler, and N. Provatas, “Modeling structural transformations in binary alloys with phase field crystals,” *Phys. Rev. B - Condens. Matter Mater. Phys.*, vol. 84, no. 6, pp. 1–10, 2011, doi: 10.1103/PhysRevB.84.064104.

[22] T. A. Grimm, “3D Printer Benchmark: North American Edition,” *TA Grimm Assoc. Inc, www. tagrimm. com*, 2010.

[23] J.-P. Kruth, “Material incress manufacturing by rapid prototyping techniques,” *CIRP Ann.*, vol. 40, no. 2, pp. 603–614, 1991.

[24] T. Sercombe, N. Jones, R. Day, and A. Kop, “Heat treatment of Ti-6Al-7Nb components produced by selective laser melting,” *Rapid Prototyp. J.*, vol. 14, no. 5, pp. 300–304, 2008.

[25] S. Biamino *et al.*, “Electron beam melting of Ti–48Al–2Cr–2Nb alloy: Microstructure and mechanical properties investigation,” *Intermetallics*, vol. 19,

no. 6, pp. 776–781, 2011.

[26] J. A. Slotwinski, E. J. Garboczi, and K. M. Hebenstreit, “Porosity measurements and analysis for metal additive manufacturing process control,” *J. Res. Natl. Inst. Stand. Technol.*, vol. 119, p. 494, 2014.

[27] S. K. Everton, M. Hirsch, P. Stravroulakis, R. K. Leach, and A. T. Clare, “Review of in-situ process monitoring and in-situ metrology for metal additive manufacturing,” *Mater. Des.*, vol. 95, pp. 431–445, 2016.

[28] H. Gong, K. Rafi, H. Gu, T. Starr, and B. Stucker, “Analysis of defect generation in Ti–6Al–4V parts made using powder bed fusion additive manufacturing processes,” *Addit. Manuf.*, vol. 1, pp. 87–98, 2014.

[29] T. Vilaro, C. Colin, and J.-D. Bartout, “As-fabricated and heat-treated microstructures of the Ti-6Al-4V alloy processed by selective laser melting,” *Metall. Mater. Trans. A*, vol. 42, no. 10, pp. 3190–3199, 2011.

[30] L. Thijs, F. Verhaeghe, T. Craeghs, J. Van Humbeeck, and J.-P. Kruth, “A study of the microstructural evolution during selective laser melting of Ti–6Al–4V,” *Acta Mater.*, vol. 58, no. 9, pp. 3303–3312, 2010.

[31] G. K. Lewis and E. Schlienger, “Practical considerations and capabilities for laser assisted direct metal deposition,” *Mater. Des.*, vol. 21, no. 4, pp. 417–423, 2000, doi: https://doi.org/10.1016/S0261-3069(99)00078-3.

[32] Q. Jia and D. Gu, “Selective laser melting additive manufacturing of Inconel 718 superalloy parts: Densification, microstructure and properties,” *J. Alloys Compd.*, vol. 585, pp. 713–721, 2014.

[33] S. Pogson, P. Fox, W. O’Neill, and C. J. Sutcliffe, “The direct metal laser remelting of copper and tool steel powders,” *Mater. Sci. Eng. A*, vol. 386, no. 1–2, pp. 453–459, 2004.

[34] L. M. Sochalski-Kolbus *et al.*, “Comparison of residual stresses in Inconel 718 simple parts made by electron beam melting and direct laser metal sintering,” *Metall. Mater. Trans. A*, vol. 46, no. 3, pp. 1419–1432, 2015.

[35] A. H. Maamoun, Y. F. Xue, M. A. Elbestawi, and S. C. Veldhuis, “Effect of selective laser melting process parameters on the quality of al alloy parts: Powder characterization, density, surface roughness, and dimensional accuracy,” *Materials (Basel).*, vol. 11, no. 12, 2018, doi: 10.3390/ma11122343.

[36] D. L. Bourell, H. L. Marcus, J. W. Barlow, and J. J. Beaman, “Selective laser sintering of metals and ceramics,” *Int. J. Powder Metall. (Princeton, New Jersey)*, vol. 28, no. 4, pp. 369–381, 1992.

[37] P. Gao, Z. Wang, and X. Zeng, “Effect of process parameters on morphology,

sectional characteristics and crack sensitivity of Ti-40Al-9V-0.5Y alloy single tracks produced by selective laser melting," *Int. J. Light. Mater. Manuf.*, 2019, doi: https://doi.org/10.1016/j.ijlmm.2019.04.001.

[38] E. Yasa, J.-P. Kruth, and J. Deckers, "Manufacturing by combining selective laser melting and selective laser erosion/laser re-melting," *CIRP Ann.*, vol. 60, no. 1, pp. 263–266, 2011.

[39] E. Yasa and J.-P. Kruth, "Microstructural investigation of Selective Laser Melting 316L stainless steel parts exposed to laser re-melting," *Procedia Eng.*, vol. 19, pp. 389–395, 2011.

[40] P. Mercelis and J. Kruth, "Residual stresses in selective laser sintering and selective laser melting," *Rapid Prototyp. J.*, 2006.

[41] M. F. Zaeh and G. Branner, "Investigations on residual stresses and deformations in selective laser melting," *Prod. Eng.*, vol. 4, no. 1, pp. 35–45, 2010, doi: 10.1007/s11740-009-0192-y.

[42] B. A. Szost *et al.*, "A comparative study of additive manufacturing techniques: Residual stress and microstructural analysis of CLAD and WAAM printed Ti-6Al-4V components," *Mater. Des.*, vol. 89, no. December, pp. 559–567, 2016, doi: 10.1016/j.matdes.2015.09.115.

[43] C. Li, Z. Y. Liu, X. Y. Fang, and Y. B. Guo, "Residual Stress in Metal Additive Manufacturing," *Procedia CIRP*, vol. 71, pp. 348–353, 2018, doi: https://doi.org/10.1016/j.procir.2018.05.039.

[44] H. Krauss, C. Eschey, and M. Zaeh, "Thermography for monitoring the selective laser melting process," in *Proceedings of the Solid Freeform Fabrication Symposium*, 2012, pp. 999–1014.

[45] G. Tapia and A. Elwany, "A review on process monitoring and control in metal-based additive manufacturing," *J. Manuf. Sci. Eng.*, vol. 136, no. 6, p. 60801, 2014.

[46] P. Aggarangsi and J. L. Beuth, "Localized preheating approaches for reducing residual stress in additive manufacturing," in *Proc. SFF Symp., Austin*, 2006, pp. 709–720.

[47] A. Vasinonta, J. L. Beuth, and M. Griffith, "Process maps for predicting residual stress and melt pool size in the laser-based fabrication of thin-walled structures," *J. Manuf. Sci. Eng*, vol. 129, no. 1, 2007.

[48] J. Li *et al.*, "Effect of stress-relief annealing on anodic dissolution behaviour of additive manufactured Ti-6Al-4V via laser solid forming," *Corros. Sci.*, vol. 153, pp. 314–326, 2019, doi: https://doi.org/10.1016/j.corsci.2019.04.002.

[49] J. D. Roehling *et al.*, “Reducing residual stress by selective large-area diode surface heating during laser powder bed fusion additive manufacturing,” *Addit. Manuf.*, vol. 28, pp. 228–235, 2019, doi: https://doi.org/10.1016/j.addma.2019.05.009.

[50] A. S. Wu, D. W. Brown, M. Kumar, G. F. Gallegos, and W. E. King, “An experimental investigation into additive manufacturing-induced residual stresses in 316L stainless steel,” *Metall. Mater. Trans. A*, vol. 45, no. 13, pp. 6260–6270, 2014.

[51] N. C. Levkulich, S. L. Semiatin, J. E. Gockel, J. R. Middendorf, A. T. DeWald, and N. W. Klingbeil, “The effect of process parameters on residual stress evolution and distortion in the laser powder bed fusion of Ti-6Al-4V,” *Addit. Manuf.*, vol. 28, pp. 475–484, 2019, doi: https://doi.org/10.1016/j.addma.2019.05.015.

[52] J. L. Beuth, “Process Maps for Predicting Residual Stress and Melt Pool Size in the Laser-Based Fabrication of Thin-Walled,” vol. 129, no. February, pp. 101–109, 2007, doi: 10.1115/1.2335852.

[53] H. L. Wei, J. Mazumder, and T. DebRoy, “Evolution of solidification texture during additive manufacturing,” *Sci. Rep.*, vol. 5, p. 16446, 2015.

[54] J. Gockel, J. Beuth, and K. Taminger, “Integrated control of solidification microstructure and melt pool dimensions in electron beam wire feed additive manufacturing of Ti-6Al-4V,” *Addit. Manuf.*, vol. 1–4, pp. 119–126, 2014, doi: https://doi.org/10.1016/j.addma.2014.09.004.

[55] S. S. Al-Bermani, M. L. Blackmore, W. Zhang, and I. Todd, “The origin of microstructural diversity, texture, and mechanical properties in electron beam melted Ti-6Al-4V,” *Metall. Mater. Trans. a*, vol. 41, no. 13, pp. 3422–3434, 2010.

[56] A. A. Antonysamy, J. Meyer, and P. B. Prangnell, “Effect of build geometry on the β-grain structure and texture in additive manufacture of Ti6Al4V by selective electron beam melting,” *Mater. Charact.*, vol. 84, pp. 153–168, 2013.

[57] G. P. Dinda, A. K. Dasgupta, and J. Mazumder, “Texture control during laser deposition of nickel-based superalloy,” *Scr. Mater.*, vol. 67, no. 5, pp. 503–506, 2012.

[58] T. Niendorf, S. Leuders, A. Riemer, H. A. Richard, T. Tröster, and D. Schwarze, “Highly anisotropic steel processed by selective laser melting,” *Metall. Mater. Trans. B*, vol. 44, no. 4, pp. 794–796, 2013.

[59] P. Kanagarajah, F. Brenne, T. Niendorf, and H. J. Maier, “Inconel 939 processed by selective laser melting: Effect of microstructure and temperature on the mechanical properties under static and cyclic loading,” *Mater. Sci. Eng. A*, vol. 588, pp. 188–195, 2013, doi: https://doi.org/10.1016/j.msea.2013.09.025.

[60] F. Yan, W. Xiong, and E. Faierson, “Grain structure control of additively manufactured metallic materials,” *Materials (Basel).*, vol. 10, no. 11, p. 1260, 2017.

[61] J. K. Holmen, J. Johnsen, S. Jupp, O. S. Hopperstad, and T. Børvik, “Effects of heat treatment on the ballistic properties of AA6070 aluminium alloy,” *Int. J. Impact Eng.*, vol. 57, pp. 119–133, 2013, doi: https://doi.org/10.1016/j.ijimpeng.2013.02.002.

[62] C.-M. Kuo and C.-W. Tsai, “Effect of cellular structure on the mechanical property of Al0.2Co1.5CrFeNi1.5Ti0.3 high-entropy alloy,” *Mater. Chem. Phys.*, vol. 210, pp. 103–110, 2018, doi: https://doi.org/10.1016/j.matchemphys.2017.10.064.

[63] H. B. Dong and P. D. Lee, “Simulation of the columnar-to-equiaxed transition in directionally solidified Al–Cu alloys,” *Acta Mater.*, vol. 53, no. 3, pp. 659–668, 2005, doi: https://doi.org/10.1016/j.actamat.2004.10.019.

[64] B. Willers, S. Eckert, U. Michel, I. Haase, and G. Zouhar, “The columnar-to-equiaxed transition in Pb–Sn alloys affected by electromagnetically driven convection,” *Mater. Sci. Eng. A*, vol. 402, no. 1, pp. 55–65, 2005, doi: https://doi.org/10.1016/j.msea.2005.03.108.

[65] Y.-Y. Zhu, H.-B. Tang, Z. Li, C. Xu, and B. He, “Solidification behavior and grain morphology of laser additive manufacturing titanium alloys,” *J. Alloys Compd.*, vol. 777, pp. 712–716, 2019, doi: https://doi.org/10.1016/j.jallcom.2018.11.055.

[66] M. J. Bermingham, D. H. StJohn, J. Krynen, S. Tedman-Jones, and M. S. Dargusch, “Promoting the columnar to equiaxed transition and grain refinement of titanium alloys during additive manufacturing,” *Acta Mater.*, vol. 168, pp. 261–274, 2019, doi: https://doi.org/10.1016/j.actamat.2019.02.020.

[67] P. Mahoney, C. J. Smith, J. Donoghue, and I. Todd, “Additive manufacturing titanium components with isotropic or graded properties by hybrid electron beam melting / hot isostatic pressing powder processing,” no. October 2018, pp. 1–11, 2019, doi: 10.1038/s41598-019-40722-3.

[68] J. Akram, P. Chalavadi, D. Pal, and B. Stucker, “Understanding grain evolution in additive manufacturing through modeling,” *Addit. Manuf.*, vol. 21, pp. 255–268, 2018.

[69] H. Yin and S. D. Felicelli, “Dendrite growth simulation during solidification in the LENS process,” *Acta Mater.*, vol. 58, no. 4, pp. 1455–1465, 2010, doi: 10.1016/j.actamat.2009.10.053.

[70] V. Fallah, M. Amoorezaei, N. Provatas, S. F. Corbin, and A. Khajepour, “Phase-field simulation of solidification morphology in laser powder deposition of Ti–Nb alloys,” *Acta Mater.*, vol. 60, no. 4, pp. 1633–1646, 2012, doi:

https://doi.org/10.1016/j.actamat.2011.12.009.

[71] F. Trevisan *et al.*, "Additive manufacturing of titanium alloys in the biomedical field: processes, properties and applications," *J. Appl. Biomater. Funct. Mater.*, vol. 16, no. 2, pp. 57–67, 2018.

[72] J. Xie, V. Oancea, J. A. Hurtado, D. Systèmes, and S. Corp, "Phase Transformations in Metals during Additive Manufacturing Processes," vol. c.

[73] Q. Zhang, J. Xie, Z. Gao, T. London, D. Griffiths, and V. Oancea, "A metallurgical phase transformation framework applied to SLM additive manufacturing processes," *Mater. Des.*, vol. 166, p. 107618, 2019, doi: https://doi.org/10.1016/j.matdes.2019.107618.

[74] A. Crespo, "Modelling of heat transfer and phase transformations in the rapid manufacturing of titanium components," in *Convection and Conduction Heat Transfer*, IntechOpen, 2011.

[75] Y. Fan, Z. Yang, P. Cheng, K. Egland, Y. L. Yao, and N. York, "Ti-6Al-4V ALLOY Department of Mechanical Engineering Transactions of NAMRI / SME Transactions of NAMRI / SME," vol. 33, pp. 235–242, 2005.

[76] J. Wang, Z. Pan, G. Yang, J. Han, X. Chen, and H. Li, "Location dependence of microstructure, phase transformation temperature and mechanical properties on Ni-rich NiTi alloy fabricated by wire arc additive manufacturing," *Mater. Sci. Eng. A*, vol. 749, pp. 218–222, 2019, doi: https://doi.org/10.1016/j.msea.2019.02.029.

[77] P. R. Halani, I. Kaya, Y. C. Shin, and H. E. Karaca, "Phase transformation characteristics and mechanical characterization of nitinol synthesized by laser direct deposition," *Mater. Sci. Eng. A*, vol. 559, pp. 836–843, 2013, doi: https://doi.org/10.1016/j.msea.2012.09.031.

[78] K. Momeni and V. I. Levitas, "Propagating phase interface with intermediate interfacial phase: phase field approach," *Phys. Rev. B*, vol. 89, no. 18, p. 184102, 2014.

[79] J. S. Lee, S. G. Kim, W. T. Kim, and T. Suzuki, "Numerical simulation of peritectic reaction using a multi-phase-field model," *ISIJ Int.*, vol. 39, no. 7, pp. 730–736, 1999, [Online]. Available: http://search.proquest.com/docview/27055414?accountid=26865.

[80] S. G. Kim, W. T. Kim, and T. Suzuki, "Interfacial compositions of solid and liquid in a phase-field model with finite interface thickness for isothermal solidification in binary alloys," *Phys. Rev. E - Stat. Physics, Plasmas, Fluids, Relat. Interdiscip. Top.*, vol. 58, no. 3, pp. 3316–3323, 1998, doi: 10.1103/PhysRevE.58.3316.

[81] V. I. Levitas, D. L. Preston, and D. W. Lee, "Three-dimensional Landau theory for multivariant stress-induced martensitic phase transformations. III. Alternative

potentials, critical nuclei, kink solutions, and dislocation theory," *Phys. Rev. B - Condens. Matter Mater. Phys.*, vol. 68, no. 13, pp. 1–24, 2003, doi: 10.1103/PhysRevB.68.134201.

[82] N. A. Ahmad, A. A. Wheeler, W. J. Boettinger, and G. B. McFadden, "Solute trapping and solute drag in a phase-field model of rapid solidification," *Phys. Rev. E - Stat. Physics, Plasmas, Fluids, Relat. Interdiscip. Top.*, vol. 58, no. 3, pp. 3436–3450, 1998, doi: 10.1103/PhysRevE.58.3436.

[83] S. G. Kim, W. T. Kim, and T. Suzuki, "Phase-field model for binary alloys," *Phys. Rev. e*, vol. 60, no. 6, p. 7186, 1999.